Novel Ultrabright and Air-Stable Photocathodes Discovered from Machine Learning and Density Functional Theory Driven Screening

Evan R. Antoniuk[*], *Peter Schindler, W. Andreas Schroeder, Bruce Dunham, Piero Pianetta, Theodore Vecchione and Evan J. Reed*[*]

E. R. Antoniuk
Stanford University, Department of Chemistry, Stanford, California, 94305, USA
E-mail: eantoniu@stanford.edu

Dr. P. Schindler
Stanford University, Department of Materials Science and Engineering, Stanford, California, 94305, USA
University of Vienna, Faculty of Physics, Vienna, Austria

Prof. W. A. Schroeder
University of Illinois at Chicago, Department of Physics, Chicago, Illinois 60607, USA

Dr. B. Dunham, Prof. P. Pianetta, Dr. T. Vecchione
SLAC, Menlo Park, California 94025, USA

Prof. E. J. Reed
Stanford University, Department of Materials Science and Engineering, Stanford, California, 94305, USA
E-mail: evanreed@stanford.edu

Keywords: photocathodes, materials discovery, work functions, free-electron lasers, photonics

The high brightness, low emittance electron beams achieved in modern x-ray free-electron lasers (XFELs) have enabled powerful X-ray imaging tools, allowing molecular systems to be imaged at picosecond time scales and sub-nanometer length scales. One of the most promising directions for increasing the brightness of XFELs is through the development of novel photocathode materials. Whereas past efforts aimed at discovering photocathode materials have typically employed trial-and-error based iterative approaches, this work represents the first data-driven screening for high brightness photocathode materials. Through screening over 74,000 semiconducting materials, a vast photocathode dataset is generated, resulting in statistically meaningful insights into the nature of high brightness photocathode materials. This screening results in a diverse list of photocathode materials that exhibit intrinsic emittances that are up to 4x lower than currently used photocathodes. In a second effort, multi-objective screening is employed to identify the family of M_2O (M=Na,K,Rb) that exhibits photoemission properties that are comparable to the current state-of-the-art

photocathode materials, but with superior air stability. This family represents perhaps the first intrinsically bright, visible light photocathode materials that are resistant to reactions with oxygen, allowing for their transport and storage in dry air environments.

1. Introduction

Upon first operation in 2009, the X-ray free electron laser (XFEL) developed at SLAC National Accelerator Laboratory achieved a peak brightness that was ten orders of magnitude larger than synchrotron sources at the time.[1] Since then, the nanoscale wavelength and femtosecond timescale pulses generated by XFELs have provided researchers with the first direct observations of atomic-level fundamental processes.[2–4] As a result of the impressive capabilities and results achieved by these XFELs, a rapid development of new XFELs has occurred globally, with the launch of three new facilities in the past three years alone.[5–7]

Relations have been derived that relate the X-ray performance of an XFEL to its electron beam brightness,[8] which is dependent upon the transverse momentum spread of electrons at the photocathode. Accordingly, the discovery of novel high brightness photocathode materials is one of the most promising directions for future XFEL performance improvements. Recent simulations of photoinjector brightness demonstrate that identifying novel photocathode materials could increase their brightness, and consequently that of XFELs, by up to two orders of magnitude.[9]

Despite the large potential increase in beam brightness that can be realized from discovering new ultrabright photocathode materials, a relatively small number of photocathode materials have been experimentally explored. The time-intensive and challenging nature of measuring the electron beam brightness from photocathode materials has limited experimental studies to only focus on less than 20 materials.[10] Similarly, performing detailed ab-initio studies of photoemission properties is computationally expensive, even for tens of photocathode materials.[11–13] With the recent development of massive materials databases, computationally screening for materials with desirable properties is a powerful new tool for accelerating materials discovery.[14–16]

In this work, we present two large-scale and comprehensive computational screenings for novel high brightness photocathode materials. In the first screening, we seek to identify the photocathode materials in our database with the highest probability of experimentally exhibiting an ultralow intrinsic emittance. Then, the second screening utilizes multi-objective screening to identify high brightness photocathode materials, that are also photo-responsive to

visible light and are resistant against oxidation. In both screenings, our workflow is constructed to provide robust predictions by explicitly accounting for the uncertainty of computational quantities that can considerably differ from experimental measurements, such as band gap and work function. Finally, we analyze our diverse dataset of tens of thousands of material properties to provide statistically-motivated insights about how to more efficiently search for ultrabright photocathode materials.

2. Identifying High Brightness Photoemitting Materials

Materials screening approaches seek to identify a set of promising candidate materials that satisfy a list of desirable criteria. Although there is considerable flexibility in the choice of criteria and how those criteria are evaluated, we utilize a few guiding principles to shape our screening workflow. First, our screening workflow is constructed of sequentially applied filters of increasing computational expense. This approach enables rapid and efficient identification of materials by ensuring that computationally expensive criteria are only applied to the most promising candidates, rather than the full dataset of materials.

Second, we construct our initial filters to efficiently screen through tens of thousands of materials by utilizing simple, but physically motivated approximations. We construct these initial approximations to consider the best-case scenario for each material, which thereby minimizes the number of false negative predictions. This principle is crucial because the initial use of a strict criteria may result in filtering out promising candidates early in the screening, which completely prevents these materials from being discovered. Our approach therefore identifies an upper limit of all photocathode materials that may be able to achieve high brightness, which then serves as a base for further down-selection with increasingly accurate calculations (**Figure 1**).

Finally, the most important part of developing a material screening workflow is the validation of the newly discovered materials. For every candidate material discovered in this work, we perform a validation of the materials' properties in a manner that is independent of our choice of screening criteria. Our initial screening criteria is simply a tool to accelerate materials discovery by identifying a shortlist of candidate photocathode materials, whereas the performance of these top candidates is subsequently established with methods that do not depend on the screening process.

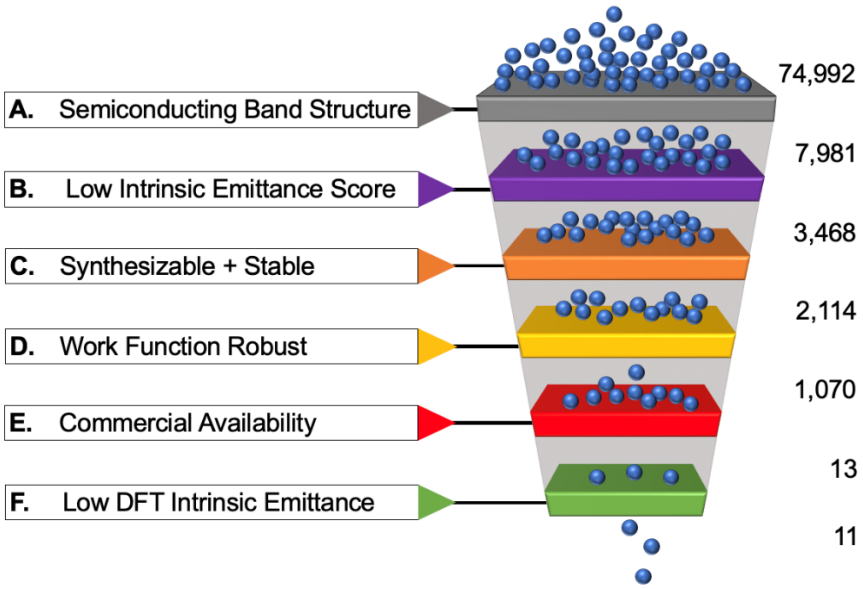


Figure 1. Screening workflow for identifying low intrinsic emittance materials. The column on the right indicates the number of remaining candidate materials after applying each screening criterion.

2.1. Identifying Semiconducting Photocathodes

XFEL photocathodes should have high quantum efficiency (QE), low intrinsic emittance, fast response time, and should be sufficiently stable to allow for sustained operation.[17] Metallic photocathodes such as Cu and Mg are commonly used because of their long operational lifetime, fast response times, ease of synthesis and reasonably low intrinsic emittance.[18–20] However, the high reflectivity and small electron-electron scattering mean free path in metals fundamentally limits their possible QE, with a peak QE of 0.3% observed in Mg.[21] Semiconducting alkali antimonide photocathodes such as Na_2KSb and Cs_3Sb were first discovered from pioneering photoemission studies by Sommer in the 1950s and remain among the most popular choice of photocathode materials today, primarily because of their impressively high QE (reaching over 40%) and relatively short response times.[22,23] However, alkali antimonide semiconductor photocathodes are extremely sensitive to oxidation. They typically require operation under ultra-high vacuum conditions and can experience a degradation in QE, even after a few minutes of operation.[24] Since the QE of metallic photocathodes are typically orders of magnitude less than that of semiconducting photocathodes, we focus our efforts on identifying a full spectrum of semiconducting photocathode materials.

To begin our screening, we identify all semiconducting materials available on the Materials Project database, a publicly available computational database containing the thermodynamic, structural, and electronic properties of over 120,000 inorganic crystalline materials, as of December 2020.[15] Among these, 74,992 materials have calculated electronic band structures available. We then identify all semiconducting materials (calculated band gap > 0eV) that have less than 20 atoms in the primitive unit cell, resulting in 13,368 unique materials. We choose to place a limit on the number of atoms in the primitive unit cell to filter out materials with overly complex structures that may be difficult to synthesize and characterize. We also eliminate all materials with spin-polarized band structures, since current DFT-based intrinsic emittance models have not been formulated to account for electronic band structures with non-degenerate spin states. These filters result in a list of 7,981 semiconducting materials that we use to search for high brightness photocathode materials.

2.2. Low Intrinisic Emittance Scores

Intrinsic emittance, ε_{int}, is the standard metric for assessing the brightness that a photocathode material can achieve. If the momentum and position of the photoemitted electrons are uncorrelated, ε_{int} is given by:

$$\varepsilon_{int} = \frac{1}{mc}\sqrt{\langle p_x^2 \rangle} \tag{1}$$

where m is the electron mass, c is the speed of light, and p_x is the transverse momentum of electrons emitted from the photocathode material (see Supplementary Note 1). During the transmission of electrons across the photocathode-vacuum interface, the transverse momentum of electrons is conserved. Therefore, the distribution of wavevectors in momentum space, as given by electronic band structures, provides a means for estimating the intrinsic emittance of a material. The relationship between the electronic band structure of a material and the intrinsic emittance calculated from that band structure is illustrated in **Figure 2**. In short, the incident photon energy dictates the states that can undergo optical excitations and the work function of the photocathode sets a lower bound on the energy of the conduction band states that can emit electrons.

Recently, Antoniuk et al. developed a DFT-based framework for calculating the intrinsic emittance of photocathode materials.[25] This method is particularly well suited for screening thousands of materials since it does not require any empirical parameters (such as electron effective mass or band gap) as inputs and was developed to be applied to a broad spectrum of

photocathode materials. In combination with the recent development of massive databases of calculated electronic band structures, this method enables the accurate determination of the intrinsic emittance for tens of thousands of candidate materials. Additional details regarding this method are given in **Supplementary Note 1**.

As shown in Figure 2, if all thermal effects are ignored, the intrinsic emittance is zero when the incident photon energy is below the photoemission threshold and typically increases monotonically as a function of photon energy when above the photoemission threshold. Therefore, searching for low emittance materials based on the minimum intrinsic emittance value is unlikely to provide meaningful results. Instead, we define a quantity that we call the intrinsic emittance score (s_{ie}) to use as a convenient metric for identifying materials that may exhibit low intrinsic emittance. To calculate s_{ie}, we first bin the intrinsic emittance values into 0.05eV intervals by taking the maximum of each interval. s_{ie} is then defined as the lowest non-zero intrinsic emittance value among all of these bins (**Figure S1**). Formulating s_{ie} in this manner is extremely convenient because the value of s_{ie} is invariant to shifts in band gap values, as can be seen by comparing the same-colored lines in Figure 2. As a result, utilizing s_{ie} allows us to identify low intrinsic emittance photocathode materials despite the well-known underestimation of the Materials Project band gaps that are calculated with the semi-local Perdew-Burke-Erzenhof (PBE) functional.[26,27] We also note that the Materials Project utilizes GGA+U electronic structure calculations for Co, Cr, Fe, Mn, Mo, Ni, V, and W oxide systems. Although s_{ie} is a predictive and convenient screening metric for identifying low intrinsic emittance materials, but should not be interpreted as a quantity that can be directly compared to experimental measurements. We further validate the use of this metric in Section 5.2 and **Supplementary Note 2**.

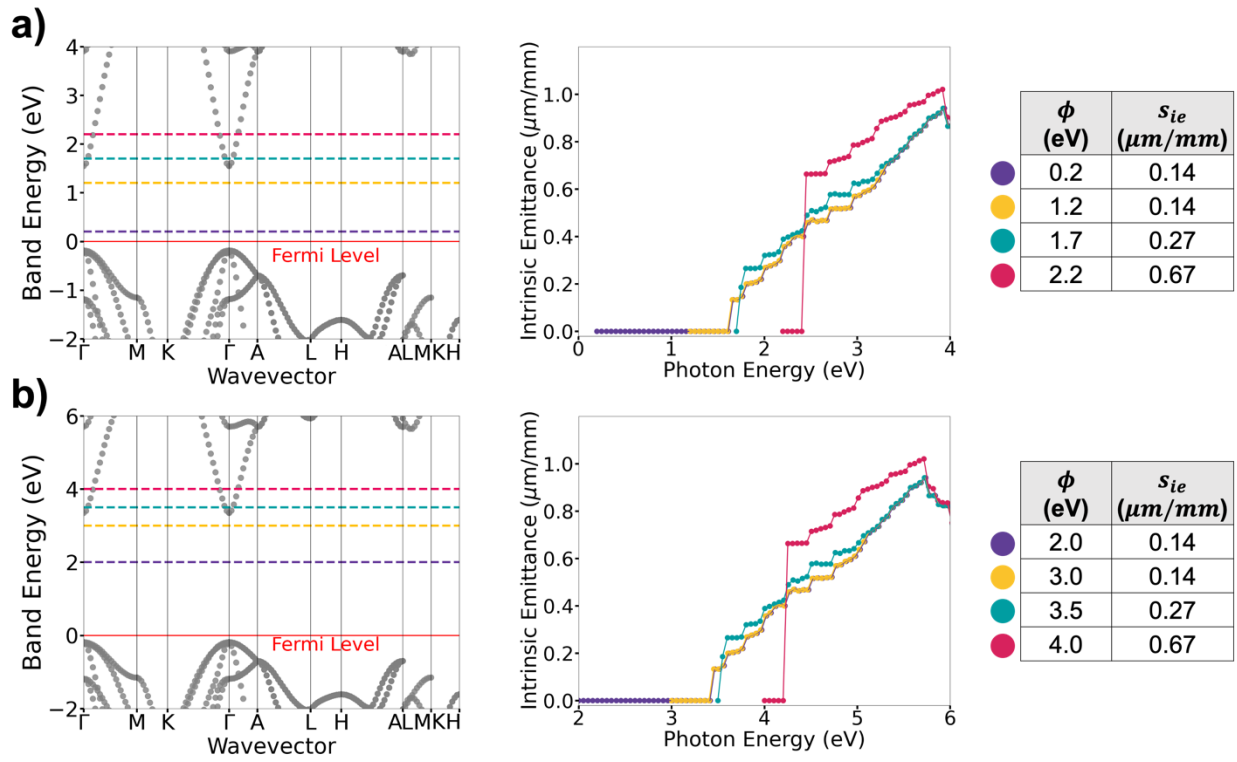


Figure 2. Calculated intrinsic emittance (ε_{int}) and intrinsic emittance scores (s_{ie}) for the prototypical semiconductor, wurtzite-GaN, plotted with various hypothetical work function values(ϕ). Left Column: Bulk electronic band structure of wurtzite-GaN obtained from a) the Materials Project database calculated with the PBE functional and b) the Materials Project with the band gap fit to the experimentally measured band gap of 3.50eV.[28] Notably, the value of s_{ie} does not change for different band gap values in the case of a fixed vacuum level, relative to the conduction band minimum (compare same colored s_{ie} values in a) and b)) However, the underestimation of the band gap will also lead to an underestimation of the photon energy and work function required for low intrinsic emittance. The vacuum level corresponding to different work function values (ϕ) are shown as dashed horizontal lines. The work function of 1.2eV in a) corresponds to the value used in our screening. Middle Column: ε_{int} calculated as a function of incident photon energy for various hypothetical work function values. The intrinsic emittance is evaluated with an incident photon energy spacing of 0.05eV. Right Column: intrinsic emittance score (s_{ie}) obtained for each hypothetical work function value.

Since the work function (ϕ) of the materials in our database depends on the surface termination of the crystal and is not known a priori, we initially take $\phi = max(E_{CBM} - 0.5\text{eV}, 0\text{eV})$, where E_{CBM} is the energy of the conduction band minimum, relative to the Fermi level (Supplementary

Note 2). Representing ϕ in this way can be considered the most optimistic choice of ϕ, since it allows all conduction band states to potentially contribute to photoemission, thus maximizing the number of materials that can have low intrinsic emittance. This optimistic choice of ϕ is desirable for an early stage of the screening process because it identifies all materials that have the potential for low emittance. As illustrated in Figure 2b), assuming a moderate work function of $\phi = 4.0$eV for GaN in our screening would prevent us from discovering the low intrinsic emittance that is possible at lower values of ϕ.

By utilizing these approximations, we determine the intrinsic emittance score for all 7,981 semiconducting materials that were identified in Section 2.1. The distribution of the results of these calculations are given in **Figure 3**. For the purposes of this screening, we consider a material to have low intrinsic emittance if it has $s_{ie} \leq 0.3\mu m\, mm^{-1}$. For comparison, commonly used Cs_2Te and K_2CsSb photocathodes operate with intrinsic emittances in the range of 0.4-0.6μm mm^{-1}.[29–31] Remarkably, we find that 3,468 materials in our database meet this low intrinsic emittance score cutoff. However, we emphasize that this value represents an upper bound to the number of materials with the potential for exhibiting low intrinsic emittance.

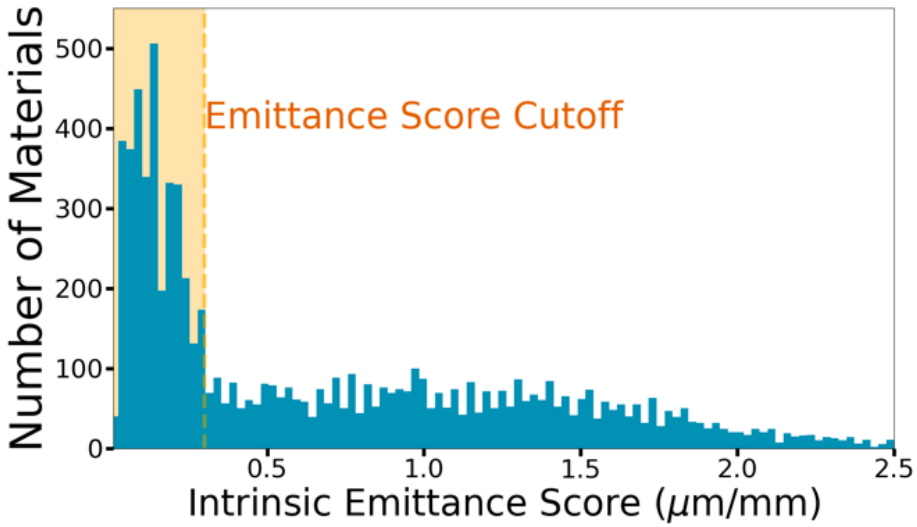


Figure 3. Distribution of intrinsic emittance scores (s_{ie}) of the 7,981 materials identified in Section 2.2. For the purpose of this screening, we classify a material as having a low intrinsic emittance if $s_{ie} \leq 0.3\mu m\, mm^{-1}$. We find that 3,468 materials in our database meet this low intrinsic emittance criteria.

2.3 Synthesizability and Thermodynamic Stability

To ensure our candidate photocathode materials can be readily integrated into photocathode-based devices, we filter out materials that have not been reported to be synthesized in the literature. For the purposes of this paper, we refer to a material as being synthesizable if that material has a previously reported synthesis in the literature. To ensure rapid implementation of our novel photocathode materials, we note that this definition of synthesizability intentionally excludes materials that are synthetically feasible, but have not yet been realized. This condition is checked by cross-referencing our candidates against the experimental synthesis information provided in the ICSD database.[14] We also verify the thermodynamic stability of our candidates through the energy above the convex hull, E_{hull}, metric provided on the Materials Project database.[15] The energy above the convex hull is defined as the formation energy of a material with respect to the most stable ground state in the chemical space of the material. This thermodynamic stability filter has previously been employed in materials screenings as a means to identify both stable and metastable candidate materials.[32–35] A recent analysis of all synthesized inorganic materials on the Materials Project database has found the 90th percentile metastability (close to being unstable) to be $67 \pm 2meV/atom$ above the convex hull that describes the lowest free energy phase(s).[35] Therefore, in accordance with our principle of identifying an upper limit to the number of possible photocathode materials, we select for materials with a calculated energy above the hull of $E_{hull} > 100\text{meV/atom}$. This choice of filter therefore captures the majority of synthesizable materials, while still eliminating synthesizable, but thermally unstable candidates.

The resulting list of 2,114 materials is noteworthy as it represents a nearly complete list of all synthesizable, bulk, inorganic semiconductor materials that may exhibit low intrinsic emittance. Despite the very low number of photocathode materials with experimentally measured low intrinsic emittance, this result seems to suggest that low intrinsic emittance may not be a rare property. However, this conclusion is dependent on how well our s_{ie} metric corresponds to experimentally measured intrinsic emittance values. In particular, this likely represents an upper bound to the number of low intrinsic emittance materials since it assumes a favorable work function value for every material.

We note that this list of 2,114 materials contains all of the known low emittance semiconducting photocathode materials that have been reported in the literature to date (Cs_3Sb, K_2CsSb, GaN, GaAs, Cs_2Te),[17] emphasizing the ability of our screening to successfully identify promising ultrabright photocathode materials. Although this list contains some

chemical analogues of these known photocathode materials, the full spectrum of identified materials is diverse and 98.3% of the materials do not belong to any known family of photocathode materials **(Table S1**). It is therefore unlikely that these novel photocathode materials could have been discovered through chemical analogy.

3. Discovery of Ultralow Emittance Photocathode Materials

In the previous section, we have identified a diverse spectrum of materials that have the potential to exhibit low intrinsic emittance under ideal conditions. We now seek to identify the photocathode materials in our database that can achieve lower intrinsic emittance than the current state-of-the-art photocathode materials when subject to typical FEL operating conditions.

First, we identify photocathode materials in our database that exhibit low intrinsic emittance when illuminated by photon energies between 1-5eV. This range of photon energies was chosen to match the range of photon energies typically used in photoinjectors (266nm for Cu and 532nm for K_2CsSb photocathodes),[30,36] while also accounting for the consistent underestimation of PBE calculated band gaps.[26] The work function of a material can vary heavily based on the atomic geometry of the surface, the presence of surface contaminants, or external electric fields.[37–39] To ensure that our candidate photocathode materials are robust against these variations in work function, we also screen our photocathode candidate materials to ensure that they exhibit low intrinsic emittance across a continuous range of possible work function values of at least 1.0eV (**Supplementary Note 3 and Figure S2**). A total of 1,070 materials satisfy these two criteria.

At this stage of the screening, we have identified 1,070 semiconducting materials that have low intrinsic emittance scores, are synthesizable, are thermodynamically stable, emit electrons when illuminated by photon energies between 1-5eV, and exhibit low intrinsic emittance over a 1eV range of work function values. As such, all 1,070 of these semiconducting materials appear to be promising high brightness photocathode materials. The next step is to extensively validate the properties of these top candidates since they were identified through approximate screening criteria. Since it is computationally intractable to validate all 1,070 materials, we proceed by identifying 13 materials that are commercially available. By identifying commercially available materials among our low emittance candidates, we expect these materials will already have a well understood synthesis, thereby accelerating the experimental realization of these promising materials.

For all 13 of these materials, we perform accurate DFT calculations of the intrinsic emittance that includes calculating the work function of the experimentally observed stable surface termination, calculating photoexcitation matrix elements, calculating the electronic structure with the hybrid functional of Heyd, Scuseria, and Ernzerhof (HSE06),[40] and evaluating the electronic structure using a dense, uniform k-point mesh (see Methods for details). In previous work, we have shown that intrinsic emittance predictions made from this method agree with experimental measurements with a mean absolute error of $0.044\mu m\, mm^{-1}$ across a diverse range of materials.[25] As a means of comparison, we perform analogous computations for the current state-of-the-art photocathode material, K_2CsSb.

Remarkably, we find that 11 out of 13 of these commercially available materials (BeSe, c-AlN, Li_2Te, w-AlN, ZnTe, ZnSe, MgTe, CdS, Na_2Te, GaN and GaP) have DFT calculated intrinsic emittance values below $0.30\mu m\, mm^{-1}$ when the work function is optimized (**Table S2, Figure S4**). The underestimation of the intrinsic emittance scores of the two misclassified materials (BP and Be_2C) is likely due to the exclusion of low symmetry k-points in the Materials Project band structure (Figure S4).

The 3 materials with the lowest predicted intrinsic emittance values are shown in **Figure 4b**). For an excess energy of 0.20eV, our DFT predictions suggest that CdS will exhibit an intrinsic emittance that is an impressive 4x less than that of K_2CsSb. Additionally, this ultralow emittance in CdS is sustained for a broader range of photon energies than for K_2CsSb. However, our predictions indicate that achieving this ultralow emittance in CdS will require lowering the work function to below 2.0eV. Similarly, we predict Na_2Te to achieve an intrinsic emittance 2x lower than K_2CsSb at an excess energy of 0.2eV, while only requiring a work function below 3eV. Additionally, 4 of the discovered low emittance materials (BeSe, Li_2Te, cubic AlN, and hexagonal AlN) are predicted to exhibit intrinsic emittance values below $0.30\mu m\, mm^{-1}$ without requiring any work function optimization (Figure 4a)).

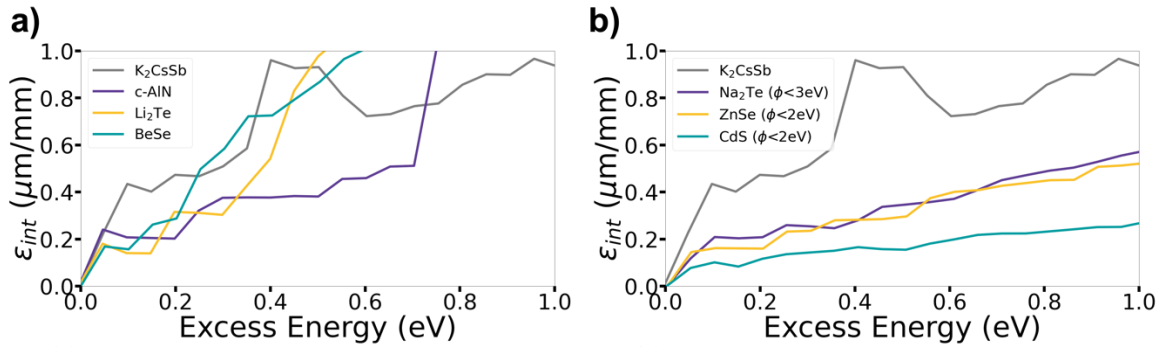


Figure 4. DFT calculated intrinsic emittance of representative examples of the ultralow emittance photocathode materials discovered in this work. The DFT calculated intrinsic emittance of the commonly used photocathode, K_2CsSb is shown for comparison. a) 3 representative examples of photocathode materials (cubic-AlN, Li_2Te and BeSe) that achieve lower intrinsic emittance than K_2CsSb without requiring work function optimization. b) 3 representative examples of photocathode materials (Na_2Te, ZnSe, and CdS) that achieve ultralow intrinsic emittance when the work function is optimized to the range of values indicated in parentheses. All 11 materials with low DFT calculated intrinsic emittance are given in Table S2.

4. Identification of Air-Stable Visible Light Photocathodes

4.1. Visible Light Photoemitters

Photocathode materials that can operate with visible light driving lasers are preferred since they can be illuminated by the second harmonic of Nd:YAG lasers and can lead to high spatial quality beams.[41] In order to identify photocathodes that exhibit low emittance when illuminated by a visible light laser, we search among the 2,114 candidates identified in Section 2.3 for materials that possess a work function below 3eV, have low intrinsic emittance for photon energies $\hbar\omega < 3$eV, and exhibit low emittance across a 1.0eV range of work function values. Setting an upper bound on the incident photon energy values required for low intrinsic emittance in this step naturally accounts for the consistent underestimation of Materials Project GGA band gaps, thus minimizing the number of false negative material predictions.[26]

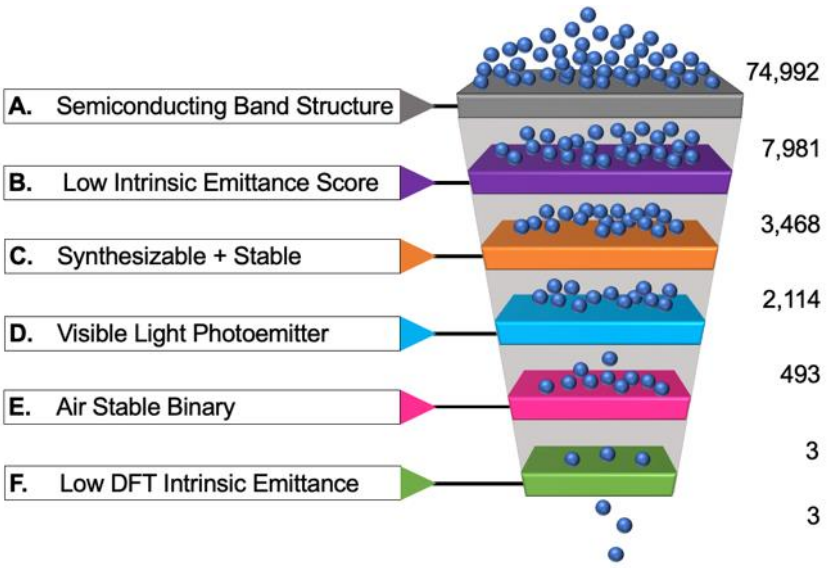


Figure 5. Screening workflow for identifying air-stable visible light photocathode materials. The column on the right indicates the number of remaining candidate materials after applying each screening criteria. Filters A-C are identical to Figure 1. However, filters D and E identify all air-stable binary materials that have low intrinsic emittance when illuminated by visible light.

In general, the work function of a material is dependent on the most stable Miller index surface termination, as well as the atomic geometry of that termination. For the 2,114 low intrinsic emittance materials identified in Section 2.3, considering all possible surface terminations up to a Miller index of 1 would require an immense 90,698 surfaces, which is an intractable number to evaluate with DFT. Instead, we utilize a recently published random forest model for predicting the work function of surfaces.[39] This model was trained on the PBE calculated work function values of 29,270 low Miller index surfaces of 2,492 crystal structures that are on the Materials Project database. Remarkably, this random forest model was shown to predict DFT-calculated work function values with a mean absolute test error of 0.19eV across a vast chemical space, which is comparable to the error between DFT-calculated and experimental work function values.[39] Notably, we can expect similar accuracy from this random forest model on our dataset since our photocathode candidates are drawn from the same database that the random forest model was tested on. Ensuring that low emittance is sustained across a 1.0eV range of possible work function values instills further confidence that our predictions are robust against the $\pm$0.19eV error that is expected in the random forest model work function predictions. With this machine learning approach, we efficiently calculate the work function

of all 90,698 surface terminations (see Methods) to identify all materials with any ϕ <3eV surface.

Applying these three criteria to the 2,114 low intrinsic emittance materials identified in Section 2.3 results in the identification of 493 low emittance, visible light photocathode materials (**Figure 5).** We note that the low work function surface terminations identified here are not checked for thermodynamic stability at this step.

Interestingly, we don't observe any significant correlation (Pearson correlation coefficient, $r = 0.010$) between the minimum work function of a material and its intrinsic emittance (**Figure S5**), suggesting that these two properties may be able to be independently engineered.

4.2. Air Stability

Beyond elucidating all possible low emittance visible light photocathodes, we now seek to identify candidate materials that can serve as air-stable replacements for alkali antimonide photocathodes. Computationally, the air stability of a material can be probed through the construction of an oxygen phase diagram. However, this method requires calculating all possible competing phases and neglects the kinetic stability of phases.[42] Instead, we hypothesize that we will be most likely to identify air stable candidate materials by searching among stable oxide materials. We emphasize that this screening strategy is aimed at targeting a chemical space that is likely to contain a high proportion of air resistant materials, whereas we rigorously establish the air stability of these materials by leveraging previous experimental reports in Section 5.1. Although there are a total of 185 oxide-containing materials in our list of 493 visible light photocathodes, we only select for binary, non-radioactive oxides for their ease of characterization and synthesis. This filter results in only 3 materials: the M_2O (M=Na,K,Rb) anti-fluorite family.

To further assess the photoemission properties of the M_2O family, we perform detailed DFT calculations to determine the intrinsic emittance for Na_2O, K_2O and Rb_2O. Our calculated properties of M_2O and K_2CsSb are well-validated by experimental values previously reported in the literature (**Table 1**) and highlight the exciting potential of the M_2O family as air-stable replacements to alkali antimonide photocathodes. In particular, we find that the M_2O family exhibits intrinsic emittance comparable to K_2CsSb (Table 1, **Figure S3**), but with the additional benefit of superior air stability. Although the presence of oxide anions in the M_2O family allow them to be stable against oxidation, their ionic nature is also likely to be responsible for the higher band gap of the M_2O family, relative to K_2CsSb (Table 1, Figure S3).

Table 1. DFT calculated and experimentally measured properties of the newly discovered Na_2O, K_2O and Rb_2O photocathode materials. The equivalent properties for K_2CsSb are shown for comparison. The intrinsic emittance scores (s_{ie}) shown here are calculated with the DFT-calculated work function (ϕ) of the experimentally observed surface termination, HSE06 electronic band structure, photoexcitation matrix elements, and a dense uniform k-point mesh. For Na_2O, K_2O and Rb_2O, the experimental and DFT work function values are with respect to the alkali-terminated (111) surface. For K_2CsSb, the experimental and DFT work function values are with respect to the Cs-terminated (111) surface.

Material	HSE-06 Band Gap (eV)	Literature Band Gap (eV)	Experiment ϕ (eV)	DFT ϕ (eV)	Electron Effective Mass (m_e)	Band Gap Type	s_{ie} ($\mu m\ mm^{-1}$)	Air Resist-ant?
Na_2O	3.26	-	1.95[43]	2.4	0.35	Direct	0.23	Yes
K_2O	2.96	-	1.75[44]	2.0	0.41	Indirect	0.19	Yes
Rb_2O	2.52	-	1.2[45]	1.1	0.36	Indirect	0.31	Yes
K_2CsSb	1.45	1.2[36]	1.8[47]	1.6	0.18	Direct	0.28	No

5. Discussion

5.1. Discussion of Discovered Photocathode Materials

There have been numerous reports of the synthesis of Na_2O thin films in the literature.[43,48,49] These syntheses typically involve thermally evaporating sodium onto a substrate, followed by controlled oxidation in a dry oxygen atmosphere. Similar reports have been made for Rb_2O and K_2O.[44,45] Electron diffraction spectra on Na_2O confirm a sodium-terminated (111) surface and subsequent field emission measurements give a work function of 1.95eV.[43] This measured work function value is in good agreement with our DFT predictions and is well below the 3.2eV work function required for low intrinsic emittance (Figure S4). Additionally, electron momentum spectroscopy (EMS) spectra taken immediately after Na_2O deposition showed no change in electronic band structure after 22 hours of exposure to the EMS electron beam.[48] To the best of our knowledge, there has been no prior studies exploring the use of any M_2O material for photoemitter applications.

These previously reported experimental findings provide convincing validation for the air stability and robustness of Na_2O. Although further experimentation is required to fully assess the lifetime of Na_2O when operated in a photoinjector and the sensitivity towards water vapor,

we expect the high air stability of the M_2O family will allow them to be operated in milder vacuum conditions and exhibit longer operational lifetimes than K_2CsSb photocathodes. The discovery of this family therefore paves the way for new photonic devices and applications that are not easily amenable to ultra-high vacuum conditions. If realized, the relaxed vacuum conditions provided by the M_2O family will also greatly simplify the fabrication, synthesis, storage, and transfer of photocathodes.

Among the 11 commercially available, low emittance photocathode materials discovered in this work, 4 are III-V semiconductors (c-AlN, w-AlN, GaN, GaP). III-V semiconducting materials such as GaN and GaAs have long been considered a promising class of photocathode materials and have demonstrated impressively high quantum efficiencies.[50,51] This work builds on this knowledge by computationally validating the low intrinsic emittance in these 4 materials, while also elucidating a complete spectrum of 14 III-V semiconductors that can be expected to exhibit low intrinsic emittance (Table S1).

The other 7 materials with low DFT-calculated intrinsic emittance are semiconducting chalcogenides (BeSe, Li_2Te, ZnTe, ZnSe, MgTe, CdS, Na_2Te). Li_2Te and Na_2Te can be considered as chemical analogues of the well-known photocathode material, Cs_2Te. BeSe, ZnTe, ZnSe, MgTe and CdS have all been previously considered in optoelectronic applications as a result of their wide band gap and low effective masses.[52–56] Interestingly, these properties are also responsible for the low predicted intrinsic emittance values in this work. The electronic properties of these materials have also been extensively studied experimentally. Our HSE06 predicted band gaps agree with experimental bands gaps with a mean absolute error of 0.28eV, providing experimental validation of the electronic structures used for the intrinsic emittance predictions in this work (Table S2). We emphasize that all 16 candidate photocathode materials studied in this work have been previously synthesized and the surface terminations were chosen based on the experimentally stable surfaces of each structure type (see Methods).

5.2. Deriving Physical Insights from Intrinsic Emittance Scores

The 16 candidate photocathode materials discovered in this work provide a means to validate the predictive power of the intrinsic emittance scores that we introduced in an empirical manner. We find that the intrinsic emittance score metric (s_{ie}) is remarkably successful at identifying low intrinsic emittance materials. 14 out of 16 (88%) of the materials with low s_{ie} were also found to exhibit low DFT-calculated intrinsic emittance values. As a result of the strong correspondence between s_{ie} and DFT-calculated intrinsic emittance values, understanding the

physical properties that are correlated with s_{ie} can provide physical insights into designing low intrinsic emittance photocathode materials.

The most frequently used method for understanding the intrinsic emittance of photocathodes is the model of Dowell-Schmerge, which predicts the intrinsic emittance to scale as $\varepsilon_{int} \propto \sqrt{m_e^*}$, where m_e^* is the electron effective mass.[36,57,58] Owing to this proportional relationship between ε_{int} and $\sqrt{m_e^*}$, previous searches for low intrinsic emittance photocathode materials have focused on identifying low electron effective mass materials with direct band gaps.[57,59,60] Notably, the Dowell-Schmerge model assumes in its derivation that the electronic structure can be represented by parabolic bands of the form, $E(\vec{k}) = E_0 + \frac{(\hbar\vec{k})^2}{2m_e^*}$, where m_e^* is taken to be isotropic. In comparison, the model that we use in this work utilizes the full electronic band structure directly, without making any assumptions about its functional form.[25] Plotting s_{ie} against m_e^* therefore allows us to quantitatively assess how well m_e^* can be used to predict intrinsic emittance across a broad spectrum of materials.

Our dataset provides some evidence that lower electron effective mass materials are more likely to exhibit low intrinsic emittance scores. On average, materials with $m_e^* < 0.2\mathrm{m_e}$ are approximately 1.3x more likely than random (58% vs. 44%) to exhibit low intrinsic emittance scores (**Figure S7, S8 and S9**). Furthermore, the average electron effective mass of the materials with DFT calculated intrinsic emittance values below $0.3\mu m\ mm^{-1}$ is $0.26\mathrm{m_e}$, which is a lower electron effective mass than 83% of the entire dataset. However, low electron effective mass is not a guarantee for low intrinsic emittance. Even among the materials with a very low electron effective mass of $m_e^* < 0.20\mathrm{m_e}$, only 58% of these materials exhibit low intrinsic emittance scores. Conversely, 19% of materials with a relatively large electron effective mass of $m_e^* > 1.00\mathrm{m_e}$ also exhibit low intrinsic emittance scores.

In agreement with the intuition that direct band gaps are needed for low emittance photocathodes, we find that direct band gap materials are approximately 1.5x more likely (59% vs 38%) to exhibit low intrinsic emittance scores than indirect band gap materials (**Table S3** and **Figure S6**). Even though direct band gap materials are more likely to exhibit low intrinsic emittance, we note that 2,035 indirect band gap materials in our database also exhibit low intrinsic emittance scores. The relative proportion of direct and indirect band gap materials that can exhibit low intrinsic emittance is expected to be affected by the exclusion of phonon scattering in our calculation of s_{ie}.

To assess how well m_e^* values can be used as a predictor for intrinsic emittance scores, we fit a square root relationship between these two quantities (**Figure S10**). However, the mean absolute error between this square root law and the calculated intrinsic emittance scores is $0.53\mu m\, mm^{-1}$. This result indicates that a very wide range of possible intrinsic emittance scores can exist for a given value of m_e^*, as is illustrated in **Figure 6**. This spread in intrinsic emittance scores may arise due to the presence of degenerate bands, non-parabolic bands and/or anisotropic bands in the electronic band structure, all of which cannot be captured by the electron effective mass parameter.

In summary, low electron effective mass materials are, on average, more likely to exhibit low intrinsic emittance scores. However, we find that electron effective mass cannot be used as a sole predictor for identifying low intrinsic emittance photocathode materials. Rather, the full electronic band structure is required to accurately model the intricate relationship between the electronic structure of a material and its intrinsic emittance.

Interestingly, we note that the well-studied photocathode materials, GaAs, K_2CsSb, and Cs_2Te, exhibit intrinsic emittance scores that are among the lowest in our entire dataset (Figure 6). Although these materials were discovered through trial-and-error based approaches and with limited data, an understanding of the physics of photoemission has allowed researchers to successfully discover a few of the brightest photocathode materials among hundreds of thousands of possible materials.

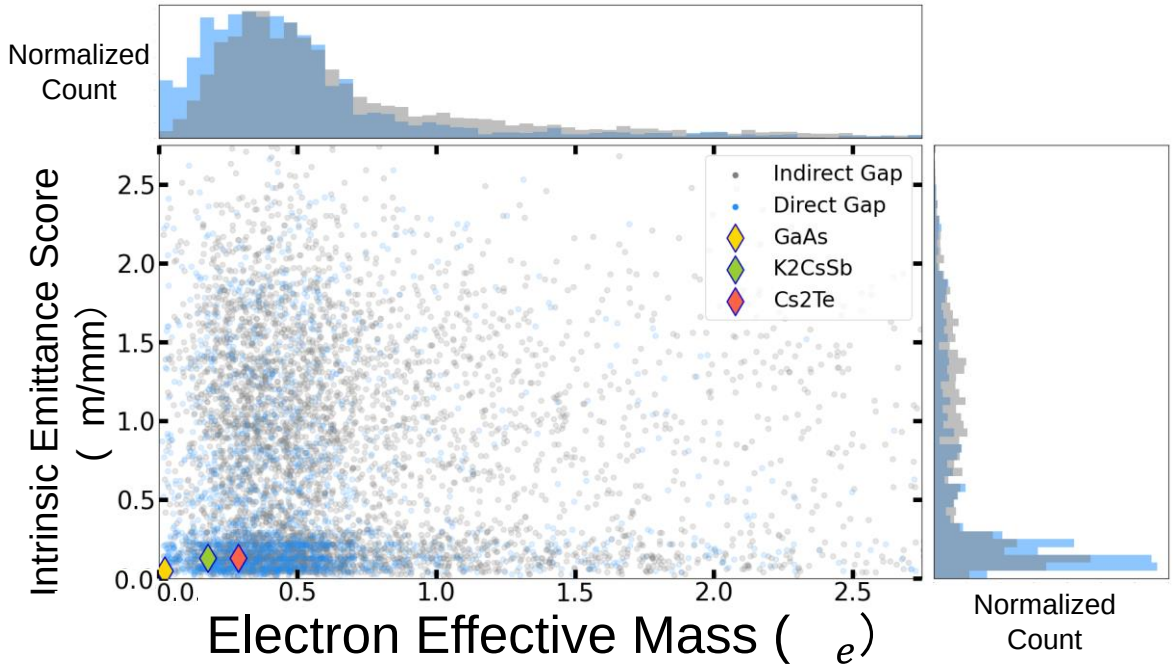


Figure 6. Calculated intrinsic emittance scores (s_{ie}) plotted against the electron effective mass for the 7,981 semiconducting candidate materials in Section 2.2. Both the intrinsic emittance scores and electron effective mass are calculated from the Materials Project band structures. Materials with direct and indirect band gaps are indicated by blue and gray, respectively, in both the scatter plot and the histogram. Calculated values for the state-of-the-art photocathode materials GaAs, K_2CsSb and Cs_2Te are shown for comparison. All categories shown in the histograms are independently normalized to account for the larger number of indirect gap materials in our database (2,084 direct gap materials and 5,897 indirect gap materials). The electron effective mass of each material is calculated from the curvature of a parabola fit to the 4 k-points on both sides of the conduction band minimum. As a result, the electron effective mass is calculated in the direction of the reciprocal space path that contains the conduction band minimum. If multiple conduction band minima are present, the minimum with the lowest electron effective mass is plotted.

5.3. Insights into Low Work Function Photocathode Materials

The traditional strategy for achieving low work function materials is to coat the surface of the material with electropositive atoms (typically cesium). This results in a reduced work function due to the build-up of electron density at the surface and the formation of surface dipoles.[61] Here, we utilize the ML predicted work functions of 90,698 surfaces to extend these

findings to the problem of identifying low work function (<3eV) photocathode materials. We find that among the low work function materials identified in this work, 53.5% contain alkali metals, 31.5% contain alkaline earth metals and 20.6% contain lanthanides (**Figure S11**). On the other hand, we find only 125 out of the 90,698 surface slabs (0.1%) had work functions below 3eV and did not contain alkali metals, alkaline earth metals or lanthanides. However, there is also no guarantee that any of these 125 low work function surfaces will be stable.

Although it is well-known that electropositive atoms are required for achieving a low work function, our results allow us to suggest that stable <3eV work function surfaces are exceedingly unlikely to exist for materials without alkali, alkaline earth or lanthanide atoms. Physically, this result may suggest that only alkali, alkaline earth, and lanthanide atoms are sufficiently electropositive to generate a large enough surface dipole that is required for a <3eV work function material. This important insight greatly reduces the search space for future searches for visible light photocathodes.

6. Conclusion

In this work, we have computationally screened 74,992 inorganic bulk materials to identify novel low emittance photocathode materials. As a result, we discover 2,114 synthesizable, low intrinsic emittance photocathode materials, serving as a rich space for future material discovery efforts. The low emittance materials discovered in this list span a diverse range of chemistries, suggesting that they could not have been discovered as chemical analogues of known photocathode materials. Our DFT validations on a subset of the discovered materials confirm the estimated low intrinsic emittance in 88% of the tested materials, highlighting the robustness of our screening predictions. Through analyzing 7,981 electronic band structures and 90,698 surface slabs, we provide statistically meaningful insights to guide future development of photocathode materials. These screening efforts also result in the identification of the M_2O family as the first air-stable visible light photocathodes, as well as ultralow emittance materials with up to 4x lower emittance than the current state-of-the-art. These discoveries are expected to greatly expand the range of experimental possibilities for photoemitting materials.

7. Methods

Machine Learning Predictions of Work Functions of Surface Slabs: The machine learning model used in this work to predict the work function of surface slabs was trained in Reference [39] on a dataset that consists of 2,492 Materials Project structures. As described in

Reference [39], these 2,492 structures were obtained by querying all elemental, binary, or ternary materials that met certain synthesis, crystal structure, and thermodynamic stability conditions. From these 2,492 structures, 29,270 unique surface terminations were generated and their work functions were calculated with the PBE exchange correlation functional. A number of machine learning models, including linear regression, neural network, and random forest models, were trained and tested with a 90/10 split of this dataset. In this work, we have chosen to utilize the random forest model to identify visible light photocathode materials since this model achieved the lowest test error among all tested models in Reference [39]. For each of the 2,114 materials identified in Section 2.3, we identify all symmetry-distinct planes with Miller indices up to a maximum of 1. For each unique Miller index, unique surface terminations are determined from the local environment criteria detailed in Reference [39]. Each of these surface slabs is then represented according to the 15 feature model described in Reference [39]. These features are comprised of various functional forms of the atomic electronegativities, atomic radii, first ionization energies, Mendeleev numbers, the packing fraction of the atomic layers, and the distances between atomic layers. The random forest model with this featurization was previously shown to predict the work function of surfaces with a mean absolute test error of 0.19eV. Notably, since our photocathode candidate materials are drawn from the same database, we expect the work function of materials in this work to be predicted with comparable accuracy. The code for this random forest model is available at https://github.com/peterschindler/WorkFunctionDatabase.

DFT Intrinsic Emittance Calculations: All DFT calculations in this work are performed with the VASP 5.4.1 package with the projector augmented-wave method.[62,63] All electronic structure calculations are relaxed until a convergence of less than 10^{-4}eV and ionic relaxations are converged to 10^{-3}eV. Plane wave basis sets are expanded with a kinetic energy cutoff that is set to be 30% larger than the VASP default values.

Calculating the intrinsic emittance requires three distinct DFT calculations. First, we calculate the electronic structure with the PBE functional by uniformly sample the first Brillouin zone on a uniform k-point mesh of at least 500 k-points per atom. For every k-point in this mesh, we also calculate the photoexcitation matrix elements, $\langle \psi_{\vec{k},c} | \vec{p} | \psi_{\vec{k},v} \rangle$. Second, we calculate the band gap with the HSE06 hybrid functional, which is expected to estimate the experimental band gap to within 0.5eV.[26,64] The intrinsic emittance is then determined from the PBE

electronic structure calculated on the uniform k-point mesh with the scissor operator applied to the electronic states to match the HSE06 band gap.[65]

Thirdly, we calculate the work function with the PBE functional and with the experimentally observed stable surface termination. We take this to be the (111) cation terminated surface for all antifluorite structures, the (110) surface for all zinc blende structures, $(10\bar{1}0)$ for all wurtzite structures and Cs-terminated (111) for K_2CsSb.[43,47,66,67] We relax the positions of the atoms in the slab for Na_2O, K_2O, Rb_2O, and K_2CsSb, and then calculate the work function for this relaxed surface slab. Due to computational expense, we calculate the work function of all other materials from slabs that have their atoms in the bulk atomic positions. For all surface slab calculations, we employ a dipole correction, include at least 15Å of vacuum space between periodic slab images, and ensure a minimum slab thickness of at least 10Å. The work function is determined from the difference between the Hartree potential in middle of the vacuum region of the computational cell and the Fermi level.

From these three calculations, the intrinsic emittance, ε_{int}, is calculated as:

$$\varepsilon_{int}(\omega,T) = \frac{\hbar}{mc}\sqrt{\sum_i w_i(\vec{k},\omega,T)k_{x,i}^2} \quad (1)$$

where w_i represents the relative probability that the i^{th} possible optical transition will result in emitting an electron with wavevector, k_x. This weight, w_i is then calculated as the product of three terms:

$$w_i(\vec{k},\omega,T) = \frac{1}{N}w_{i,kpt}(\vec{k}) \times w_{i,opt}(\vec{k},\omega,T) \times w_{i,escape}(\vec{k}) \quad (2)$$

where $w_{i,kpt}(\vec{k}), w_{i,opt}(\vec{k},\omega,T)\ and\ w_{i,escape}(\vec{k})$ represent the k-point degeneracy, the probability of photoexcitation, and the probability of photoemission from the photocathode, respectively (see Supplementary Note 1). Therefore, the electronic structure calculations performed above give the distribution of wavevectors, $\vec{k}$, necessary to evaluate all 3 of these terms. In addition, we perform HSE06 electronic structure calculations to more accurately represent the band gap of the material, which affects $w_{i,opt}(\vec{k},\omega,T)$. Finally, the work function calculation is required to evaluate $w_{i,escape}(\vec{k})$, since the work function describes the energy required for electrons to be emitted from the photocathode.

Supporting Information

Supporting Information is available from the Wiley Online Library or from the author.

Data Availability

The data that support the findings of this study are available from the corresponding author upon reasonable request.

Acknowledgements

P.S. gratefully acknowledges financial support from the Austrian Science Fund (FWF) under contract J3980-N27. This work used the Extreme Science and Engineering Discovery Environment (XSEDE) Stampede2 and Comet at the service-provider through allocation DMR190060, which is supported by National Science Foundation grant number ACI-1548562. This work was supported in part by the U.S. Department of Energy, Laboratory Directed Research and Development program at SLAC National Accelerator Laboratory, under contract No. DE-AC02-76SF00515 and the U.S. Department of Energy, Office of Science, Office of High Energy Physics under FWP 100588, "From Theory to Practical High Brightness Photocathodes.

Conflict of Interest

E.R.A., B.D., T.V., P.P., and E.J.R. filed a patent for the high brightness photocathode materials discovered in this work.

Author Contributions

E.R.A. performed all DFT calculations, and determined the ML work function values. P.S. aided in the generation of surface slabs and the development of the work function ML model. All authors contributed to the development of the screening workflow for identifying photocathode materials. E.R.A. prepared the manuscript with feedback from all authors.

Received: ((will be filled in by the editorial staff))
Revised: ((will be filled in by the editorial staff))
Published online: ((will be filled in by the editorial staff))

References

[1] P. Emma, R. Akre, J. Arthur, R. Bionta, C. Bostedt, J. Bozek, A. Brachmann, P. Bucksbaum, R. Coffee, F.-J. Decker, Y. Ding, D. Dowell, S. Edstrom, A. Fisher, J. Frisch, S. Gilevich, J. Hastings, G. Hays, P. Hering, Z. Huang, R. Iverson, H. Loos, M. Messerschmidt, A. Miahnahri, S. Moeller, H.-D. Nuhn, G. Pile, D. Ratner, J. Rzepiela, D. Schultz, T. Smith, P. Stefan, H. Tompkins, J. Turner, J. Welch, W. White, J. Wu, G. Yocky, and J. Galayda, *First Lasing and Operation of an Ångstrom-Wavelength Free-Electron Laser*, Nat. Photonics **4**, 9 (2010).

[2] M. Cammarata, S. Zerdane, L. Balducci, G. Azzolina, S. Mazerat, C. Exertier, M. Trabuco, M. Levantino, R. Alonso-Mori, J. M. Glownia, S. Song, L. Catala, T. Mallah, S. F. Matar, and E. Collet, *Charge Transfer Driven by Ultrafast Spin Transition in a CoFe Prussian Blue Analogue*, Nat. Chem. **13**, 1 (2021).

[3] R. Dods, P. Båth, D. Morozov, V. A. Gagnér, D. Arnlund, H. L. Luk, J. Kübel, M. Maj, A. Vallejos, C. Wickstrand, R. Bosman, K. R. Beyerlein, G. Nelson, M. Liang, D. Milathianaki, J. Robinson, R. Harimoorthy, P. Berntsen, E. Malmerberg, L. Johansson, R. Andersson, S. Carbajo, E. Claesson, C. E. Conrad, P. Dahl, G. Hammarin, M. S. Hunter, C. Li, S. Lisova, A. Royant, C. Safari, A. Sharma, G. J. Williams, O. Yefanov, S. Westenhoff, J. Davidsson, D. P. DePonte, S. Boutet, A. Barty, G. Katona, G. Groenhof, G. Brändén, and R. Neutze, *Ultrafast Structural Changes within a Photosynthetic Reaction Centre*, Nature **589**, 7841 (2021).

[4] K. Ledbetter, E. Biasin, J. P. F. Nunes, M. Centurion, K. J. Gaffney, M. Kozina, M.-F. Lin, X. Shen, J. Yang, X. J. Wang, T. J. A. Wolf, and A. A. Cordones, *Photodissociation of Aqueous I 3 − Observed with Liquid-Phase Ultrafast Mega-Electron-Volt Electron Diffraction*, Struct. Dyn. **7**, 064901 (2020).

[5] H.-S. Kang, C.-K. Min, H. Heo, C. Kim, H. Yang, G. Kim, I. Nam, S. Y. Baek, H.-J. Choi, G. Mun, B. R. Park, Y. J. Suh, D. C. Shin, J. Hu, J. Hong, S. Jung, S.-H. Kim, K. Kim, D. Na, S. S. Park, Y. J. Park, J.-H. Han, Y. G. Jung, S. H. Jeong, H. G. Lee, S. Lee, S. Lee, W.-W. Lee, B. Oh, H. S. Suh, Y. W. Parc, S.-J. Park, M. H. Kim, N.-S. Jung, Y.-C. Kim, M.-S. Lee, B.-H. Lee, C.-W. Sung, I.-S. Mok, J.-M. Yang, C.-S. Lee, H. Shin, J. H. Kim, Y. Kim, J. H. Lee, S.-Y. Park, J. Kim, J. Park, I. Eom, S. Rah, S. Kim, K. H. Nam, J. Park, J. Park, S. Kim, S. Kwon, S. H. Park, K. S. Kim, H. Hyun, S. N. Kim, S. Kim, S. Hwang, M. J. Kim, C. Lim, C.-J. Yu, B.-S. Kim, T.-H. Kang, K.-W. Kim, S.-H. Kim, H.-S. Lee, H.-S. Lee, K.-H. Park, T.-Y. Koo, D.-E. Kim, and I. S. Ko, *Hard X-Ray Free-Electron Laser with Femtosecond-Scale Timing Jitter*, Nat. Photonics **11**, 11 (2017).

[6] W. Decking, S. Abeghyan, P. Abramian, A. Abramsky, A. Aguirre, C. Albrecht, P. Alou, M. Altarelli, P. Altmann, K. Amyan, V. Anashin, E. Apostolov, K. Appel, D. Auguste, V. Ayvazyan, S. Baark, F. Babies, N. Baboi, P. Bak, V. Balandin, R. Baldinger, B. Baranasic, S. Barbanotti, O. Belikov, V. Belokurov, L. Belova, V. Belyakov, S. Berry, M. Bertucci, B. Beutner, A. Block, M. Blöcher, T. Böckmann, C. Bohm, M. Böhnert, V. Bondar, E. Bondarchuk, M. Bonezzi, P. Borowiec, C. Bösch, U. Bösenberg, A. Bosotti, R. Böspflug, M. Bousonville, E. Boyd, Y. Bozhko, A. Brand, J. Branlard, S. Briechle, F. Brinker, S. Brinker, R. Brinkmann, S. Brockhauser, O. Brovko, H. Brück, A. Brüdgam, L. Butkowski, T. Büttner, J. Calero, E. Castro-Carballo, G. Cattalanotto, J. Charrier, J. Chen, A. Cherepenko, V. Cheskidov, M. Chiodini, A. Chong, S. Choroba, M. Chorowski, D. Churanov, W. Cichalewski, M. Clausen, W. Clement, C. Cloué, J. A. Cobos, N. Coppola, S. Cunis, K. Czuba, M. Czwalinna, B. D'Almagne, J. Dammann, H. Danared, A. de Zubiaurre Wagner, A. Delfs, T. Delfs, F. Dietrich, T.

Dietrich, M. Dohlus, M. Dommach, A. Donat, X. Dong, N. Doynikov, M. Dressel, M. Duda, P. Duda, H. Eckoldt, W. Ehsan, J. Eidam, F. Eints, C. Engling, U. Englisch, A. Ermakov, K. Escherich, J. Eschke, E. Saldin, M. Faesing, A. Fallou, M. Felber, M. Fenner, B. Fernandes, J. M. Fernández, S. Feuker, K. Filippakopoulos, K. Floettmann, V. Fogel, M. Fontaine, A. Francés, I. F. Martin, W. Freund, T. Freyermuth, M. Friedland, L. Fröhlich, M. Fusetti, J. Fydrych, A. Gallas, O. García, L. Garcia-Tabares, G. Geloni, N. Gerasimova, C. Gerth, P. Geßler, V. Gharibyan, M. Gloor, J. Głowinkowski, A. Goessel, Z. Gołębiewski, N. Golubeva, W. Grabowski, W. Graeff, A. Grebentsov, M. Grecki, T. Grevsmuehl, M. Gross, U. Grosse-Wortmann, J. Grünert, S. Grunewald, P. Grzegory, G. Feng, H. Guler, G. Gusev, J. L. Gutierrez, L. Hagge, M. Hamberg, R. Hanneken, E. Harms, I. Hartl, A. Hauberg, S. Hauf, J. Hauschildt, J. Hauser, J. Havlicek, A. Hedqvist, N. Heidbrook, F. Hellberg, D. Henning, O. Hensler, T. Hermann, A. Hidvégi, M. Hierholzer, H. Hintz, F. Hoffmann, M. Hoffmann, M. Hoffmann, Y. Holler, M. Hüning, A. Ignatenko, M. Ilchen, A. Iluk, J. Iversen, J. Iversen, M. Izquierdo, L. Jachmann, N. Jardon, U. Jastrow, K. Jensch, J. Jensen, M. Jeżabek, M. Jidda, H. Jin, N. Johansson, R. Jonas, W. Kaabi, D. Kaefer, R. Kammering, H. Kapitza, S. Karabekyan, S. Karstensen, K. Kasprzak, V. Katalev, D. Keese, B. Keil, M. Kholopov, M. Killenberger, B. Kitaev, Y. Klimchenko, R. Klos, L. Knebel, A. Koch, M. Koepke, S. Köhler, W. Köhler, N. Kohlstrunk, Z. Konopkova, A. Konstantinov, W. Kook, W. Koprek, M. Körfer, O. Korth, A. Kosarev, K. Kosiński, D. Kostin, Y. Kot, A. Kotarba, T. Kozak, V. Kozak, R. Kramert, M. Krasilnikov, A. Krasnov, B. Krause, L. Kravchuk, O. Krebs, R. Kretschmer, J. Kreutzkamp, O. Kröplin, K. Krzysik, G. Kube, H. Kuehn, N. Kujala, V. Kulikov, V. Kuzminych, D. La Civita, M. Lacroix, T. Lamb, A. Lancetov, M. Larsson, D. Le Pinvidic, S. Lederer, T. Lensch, D. Lenz, A. Leuschner, F. Levenhagen, Y. Li, J. Liebing, L. Lilje, T. Limberg, D. Lipka, B. List, J. Liu, S. Liu, B. Lorbeer, J. Lorkiewicz, H. H. Lu, F. Ludwig, K. Machau, W. Maciocha, C. Madec, C. Magueur, C. Maiano, I. Maksimova, K. Malcher, T. Maltezopoulos, E. Mamoshkina, B. Manschwetus, F. Marcellini, G. Marinkovic, T. Martinez, H. Martirosyan, W. Maschmann, M. Maslov, A. Matheisen, U. Mavric, J. Meißner, K. Meissner, M. Messerschmidt, N. Meyners, G. Michalski, P. Michelato, N. Mildner, M. Moe, F. Moglia, C. Mohr, S. Mohr, W. Möller, M. Mommerz, L. Monaco, C. Montiel, M. Moretti, I. Morozov, P. Morozov, D. Mross, J. Mueller, C. Müller, J. Müller, K. Müller, J. Munilla, A. Münnich, V. Muratov, O. Napoly, B. Näser, N. Nefedov, R. Neumann, R. Neumann, N. Ngada, D. Noelle, F. Obier, I. Okunev, J. A. Oliver, M. Omet, A. Oppelt, A. Ottmar, M. Oublaid, C. Pagani, R. Paparella, V. Paramonov, C. Peitzmann, J. Penning, A. Perus, F. Peters, B. Petersen, A. Petrov, I. Petrov, S. Pfeiffer, J. Pflüger, S. Philipp, Y. Pienaud, P. Pierini, S. Pivovarov, M. Planas, E. Pławski, M. Pohl, J. Polinski, V. Popov, S. Prat, J. Prenting, G. Priebe, H. Pryschelski, K. Przygoda, E. Pyata, B. Racky, A. Rathjen, W. Ratuschni, S. Regnaud-Campderros, K. Rehlich, D. Reschke, C. Robson, J. Roever, M. Roggli, J. Rothenburg, E. Rusiński, R. Rybaniec, H. Sahling, M. Salmani, L. Samoylova, D. Sanzone, F. Saretzki, O. Sawlanski, J. Schaffran, H. Schlarb, M. Schlösser, V. Schlott, C. Schmidt, F. Schmidt-Foehre, M. Schmitz, M. Schmökel, T. Schnautz, E. Schneidmiller, M. Scholz, B. Schöneburg, J. Schultze, C. Schulz, A. Schwarz, J. Sekutowicz, D. Sellmann, E. Semenov, S. Serkez, D. Sertore, N. Shehzad, P. Shemarykin, L. Shi, M. Sienkiewicz, D. Sikora, M. Sikorski, A. Silenzi, C. Simon, W. Singer, X. Singer, H. Sinn, K. Sinram, N. Skvorodnev, P. Smirnow, T. Sommer, A. Sorokin, M. Stadler, M. Steckel, B. Steffen, N. Steinhau-Kühl, F. Stephan, M. Stodulski, M. Stolper, A. Sulimov, R. Susen, J. Świerblewski, C. Sydlo, E. Syresin, V. Sytchev, J. Szuba, N. Tesch, J. Thie, A. Thiebault, K. Tiedtke, D. Tischhauser, J. Tolkiehn, S.

Tomin, F. Tonisch, F. Toral, I. Torbin, A. Trapp, D. Treyer, G. Trowitzsch, T. Trublet, T. Tschentscher, F. Ullrich, M. Vannoni, P. Varela, G. Varghese, G. Vashchenko, M. Vasic, C. Vazquez-Velez, A. Verguet, S. Vilcins-Czvitkovits, R. Villanueva, B. Visentin, M. Viti, E. Vogel, E. Volobuev, R. Wagner, N. Walker, T. Wamsat, H. Weddig, G. Weichert, H. Weise, R. Wenndorf, M. Werner, R. Wichmann, C. Wiebers, M. Wiencek, T. Wilksen, I. Will, L. Winkelmann, M. Winkowski, K. Wittenburg, A. Witzig, P. Wlk, T. Wohlenberg, M. Wojciechowski, F. Wolff-Fabris, G. Wrochna, K. Wrona, M. Yakopov, B. Yang, F. Yang, M. Yurkov, I. Zagorodnov, P. Zalden, A. Zavadtsev, D. Zavadtsev, A. Zhirnov, A. Zhukov, V. Ziemann, A. Zolotov, N. Zolotukhina, F. Zummack, and D. Zybin, *A MHz-Repetition-Rate Hard X-Ray Free-Electron Laser Driven by a Superconducting Linear Accelerator*, Nat. Photonics **14**, 6 (2020).

[7] E. Prat, R. Abela, M. Aiba, A. Alarcon, J. Alex, Y. Arbelo, C. Arrell, V. Arsov, C. Bacellar, C. Beard, P. Beaud, S. Bettoni, R. Biffiger, M. Bopp, H.-H. Braun, M. Calvi, A. Cassar, T. Celcer, M. Chergui, P. Chevtsov, C. Cirelli, A. Citterio, P. Craievich, M. C. Divall, A. Dax, M. Dehler, Y. Deng, A. Dietrich, P. Dijkstal, R. Dinapoli, S. Dordevic, S. Ebner, D. Engeler, C. Erny, V. Esposito, E. Ferrari, U. Flechsig, R. Follath, F. Frei, R. Ganter, T. Garvey, Z. Geng, A. Gobbo, C. Gough, A. Hauff, C. P. Hauri, N. Hiller, S. Hunziker, M. Huppert, G. Ingold, R. Ischebeck, M. Janousch, P. J. M. Johnson, S. L. Johnson, P. Juranić, M. Jurcevic, M. Kaiser, R. Kalt, B. Keil, D. Kiselev, C. Kittel, G. Knopp, W. Koprek, M. Laznovsky, H. T. Lemke, D. L. Sancho, F. Löhl, A. Malyzhenkov, G. F. Mancini, R. Mankowsky, F. Marcellini, G. Marinkovic, I. Martiel, F. Märki, C. J. Milne, A. Mozzanica, K. Nass, G. L. Orlandi, C. O. Loch, M. Paraliev, B. Patterson, L. Patthey, B. Pedrini, M. Pedrozzi, C. Pradervand, P. Radi, J.-Y. Raguin, S. Redford, J. Rehanek, S. Reiche, L. Rivkin, A. Romann, L. Sala, M. Sander, T. Schietinger, T. Schilcher, V. Schlott, T. Schmidt, M. Seidel, M. Stadler, L. Stingelin, C. Svetina, D. M. Treyer, A. Trisorio, C. Vicario, D. Voulot, A. Wrulich, S. Zerdane, and E. Zimoch, *A Compact and Cost-Effective Hard X-Ray Free-Electron Laser Driven by a High-Brightness and Low-Energy Electron Beam*, Nat. Photonics **14**, 12 (2020).

[8] Z. Huang and K.-J. Kim, *Review of X-Ray Free-Electron Laser Theory*, Phys. Rev. Spec. Top. - Accel. Beams **10**, 034801 (2007).

[9] C. M. Pierce, M. B. Andorf, E. Lu, M. Gordon, Y.-K. Kim, C. Gulliford, I. V. Bazarov, J. M. Maxson, N. P. Norvell, B. M. Dunham, and T. O. Raubenheimer, *The Role of Low Intrinsic Emittance in Modern Photoinjector Brightness*, Phys. Rev. Accel. Beams **23**, 070101 (2020).

[10] D. H. Dowell, I. Bazarov, B. Dunham, K. Harkay, C. Hernandez-Garcia, R. Legg, H. Padmore, T. Rao, J. Smedley, and W. Wan, *Cathode R&D for Future Light Sources*, Nucl. Instrum. Methods Phys. Res. Sect. Accel. Spectrometers Detect. Assoc. Equip. **622**, 685 (2010).

[11] R. Amador, H.-D. Saßnick, and C. Cocchi, *Electronic Structure and Optical Properties of Na2KSb and NaK2Sb from First-Principles Many-Body Theory*, J. Phys. Condens. Matter **33**, 365502 (2021).

[12] J. K. Nangoi, S. Karkare, R. Sundararaman, H. A. Padmore, and T. A. Arias, *Ab Initio Many-Body Photoemission Theory of Transverse Energy Distribution of Photoelectrons: PbTe(111) as a Case Study with Experimental Comparisons*, ArXiv200611924 Cond-Mat Physicsphysics (2020).

[13] H.-D. Saßnick and C. Cocchi, *Electronic Structure of Cesium-Based Photocathode Materials from Density Functional Theory: Performance of PBE, SCAN, and HSE06 Functionals*, Electron. Struct. **3**, 027001 (2021).

[14] I. Levin, *NIST Inorganic Crystal Structure Database (ICSD)*, https://doi.org/10.18434/M32147.
[15] A. Jain, S. P. Ong, G. Hautier, W. Chen, W. D. Richards, S. Dacek, S. Cholia, D. Gunter, D. Skinner, G. Ceder, and K. A. Persson, *Commentary: The Materials Project: A Materials Genome Approach to Accelerating Materials Innovation*, APL Mater. **1**, 011002 (2013).
[16] K. Choudhary, Q. Zhang, A. C. E. Reid, S. Chowdhury, N. Van Nguyen, Z. Trautt, M. W. Newrock, F. Y. Congo, and F. Tavazza, *Computational Screening of High-Performance Optoelectronic Materials Using OptB88vdW and TB-MBJ Formalisms*, Sci. Data **5**, 180082 (2018).
[17] *Photocathodes for High Brightness Photo Injectors*, Phys. Procedia **77**, 58 (2015).
[18] N. Gazis, E. Tanke, E. Trachanas, T. Apostolopoulos, A. Karagiannaki, K. Pramatari, I. Telali, K. Tzanetou, and E. Gazis, *Photocathode Study of the CompactLight Collaboration for a Novel XFEL Development*, Int. J. Mod. Phys. Conf. Ser. **50**, 2060007 (2020).
[19] *Measurements on Photoelectrons from a Magnesium Cathode in a Microwave Electron Gun*, Nucl. Instrum. Methods Phys. Res. Sect. Accel. Spectrometers Detect. Assoc. Equip. **356**, 159 (1995).
[20] S. Karkare, G. Adhikari, W. A. Schroeder, J. K. Nangoi, T. Arias, J. Maxson, and H. Padmore, *Ultracold Electrons via Near-Threshold Photoemission from Single-Crystal Cu(100)*, Phys. Rev. Lett. **125**, 054801 (2020).
[21] R. Xiang, A. Arnold, P. Michel, P. Murcek, J. Teichert, P. Lu, H. Vennekate, T. Dresden, and P. Patra, *IMPROVEMENT OF PHOTOEMISSION EFFICIENCY OF MAGNESIUM PHOTOCATHODES*, 3 (2017).
[22] W. E. Spicer, *Photoemissive, Photoconductive, and Optical Absorption Studies of Alkali-Antimony Compounds*, Phys. Rev. **112**, 114 (1958).
[23] W. E. Spicer, *The Production of Pairs in Semiconductors by Low Energy Electrons*, J. Phys. Chem. Solids **22**, 365 (1961).
[24] *Technological Challenges for High Brightness Photo-Injectors - INSPIRE*, https://inspirehep.net/literature/657977.
[25] E. R. Antoniuk, Y. Yue, Y. Zhou, P. Schindler, W. A. Schroeder, B. Dunham, P. Pianetta, T. Vecchione, and E. J. Reed, *Generalizable Density Functional Theory Based Photoemission Model for the Accelerated Development of Photocathodes and Other Photoemissive Devices*, Phys. Rev. B **101**, 235447 (2020).
[26] P. Borlido, J. Schmidt, A. W. Huran, F. Tran, M. A. L. Marques, and S. Botti, *Exchange-Correlation Functionals for Band Gaps of Solids: Benchmark, Reparametrization and Machine Learning*, Npj Comput. Mater. **6**, 1 (2020).
[27] J. P. Perdew, K. Burke, and M. Ernzerhof, *Generalized Gradient Approximation Made Simple*, Phys. Rev. Lett. **77**, 3865 (1996).
[28] B. Monemar, *Fundamental Energy Gap of GaN from Photoluminescence Excitation Spectra*, Phys. Rev. B **10**, 676 (1974).
[29] E. Prat, S. Bettoni, H.-H. Braun, R. Ganter, and T. Schietinger, *Measurements of Copper and Cesium Telluride Cathodes in a Radio-Frequency Photoinjector*, Phys. Rev. Spec. Top. - Accel. Beams **18**, 043401 (2015).
[30] H. A. Padmore, D. Dowell, J. Feng, T. Vecchione, and W. Wan, *High QE, Low Emittance, Green Sensitive FEL Photocathodes Using K2CsSb*, 4 (2012).
[31] I. Bazarov, L. Cultrera, A. Bartnik, B. Dunham, S. Karkare, Y. Li, X. Liu, J. Maxson, and W. Roussel, *Thermal Emittance Measurements of a Cesium Potassium Antimonide Photocathode*, Appl. Phys. Lett. **98**, 224101 (2011).

[32] G. Cheon, K.-A. N. Duerloo, A. D. Sendek, C. Porter, Y. Chen, and E. J. Reed, *Data Mining for New Two- and One-Dimensional Weakly Bonded Solids and Lattice-Commensurate Heterostructures*, Nano Lett. **17**, 1915 (2017).
[33] S. Kirklin, J. E. Saal, V. I. Hegde, and C. Wolverton, *High-Throughput Computational Search for Strengthening Precipitates in Alloys*, Acta Mater. **102**, 125 (2016).
[34] M. Aykol, S. S. Dwaraknath, W. Sun, and K. A. Persson, *Thermodynamic Limit for Synthesis of Metastable Inorganic Materials*, Sci. Adv. **4**, eaaq0148 (2018).
[35] W. Sun, S. T. Dacek, S. P. Ong, G. Hautier, A. Jain, W. D. Richards, A. C. Gamst, K. A. Persson, and G. Ceder, *The Thermodynamic Scale of Inorganic Crystalline Metastability*, Sci. Adv. **2**, e1600225 (2016).
[36] D. H. Dowell and J. F. Schmerge, *Quantum Efficiency and Thermal Emittance of Metal Photocathodes*, Phys. Rev. Spec. Top. - Accel. Beams **12**, 074201 (2009).
[37] Y.-J. Yu, Y. Zhao, S. Ryu, L. E. Brus, K. S. Kim, and P. Kim, *Tuning the Graphene Work Function by Electric Field Effect*, Nano Lett. **9**, 3430 (2009).
[38] M. G. Helander, M. T. Greiner, Z. B. Wang, and Z. H. Lu, *Pitfalls in Measuring Work Function Using Photoelectron Spectroscopy*, Appl. Surf. Sci. **256**, 2602 (2010).
[39] P. Schindler, E. R. Antoniuk, G. Cheon, Y. Zhu, and E. J. Reed, *Discovery of Materials with Extreme Work Functions by High-Throughput Density Functional Theory and Machine Learning*, ArXiv201110905 Cond-Mat Physicsphysics (2020).
[40] J. Heyd, G. E. Scuseria, and M. Ernzerhof, *Erratum: "Hybrid Functionals Based on a Screened Coulomb Potential" [J. Chem. Phys. 118, 8207 (2003)]*, J. Chem. Phys. **124**, 219906 (2006).
[41] T. Wang, T. Zhan, H. Zhu, and L. Qian, *Analysis of Beam-Quality Degradation in Nonlinear Frequency Conversion*, JOSA B **19**, 1101 (2002).
[42] S. P. Ong, L. Wang, B. Kang, and G. Ceder, *Li−Fe−P−O2 Phase Diagram from First Principles Calculations*, Chem. Mater. **20**, 1798 (2008).
[43] *Low Energy Electron Diffraction from Na(110) and Na2O(111) Surfaces*, Surf. Sci. **65**, 539 (1977).
[44] *Ionic Oxygen Species Formed in the Presence of Lithium, Potassium and Cesium*, Surf. Sci. **260**, 271 (1992).
[45] G. H. Fecher, J. Bansmann, Ch. Grünewald, A. Oelsner, Ch. Ostertag, and G. Schönhense, *Oxidation of Rubidium at Platinum (111)*, Surf. Sci. **307–309**, 70 (1994).
[46] C. Ghosh and B. P. Varma, *Preparation and Study of Properties of a Few Alkali Antimonide Photocathodes*, J. Appl. Phys. **49**, 4549 (1978).
[47] H. Yamaguchi, F. Liu, J. DeFazio, C. W. N. Villarrubia, D. Finkenstadt, A. Shabaev, K. L. Jensen, V. Pavlenko, M. Mehl, S. Lambrakos, G. Gupta, A. D. Mohite, and N. A. Moody, *Active Bialkali Photocathodes on Free-Standing Graphene Substrates*, ArXiv170300921 Cond-Mat (2017).
[48] E. A. Mikajlo, K. L. Nixon, and M. J. Ford, *Electron Momentum Spectroscopy and Linear Combination of Atomic Orbitals Calculation of Bulk Na2O*, J. Phys. Condens. Matter **15**, 2155 (2003).
[49] A. Barrie and F. J. Street, *An Auger and X-Ray Photoelectron Spectroscopic Study of Sodium Metal and Sodium Oxide*, J. Electron Spectrosc. Relat. Phenom. **7**, 1 (1975).
[50] S. Karkare, L. Boulet, L. Cultrera, B. Dunham, X. Liu, W. Schaff, and I. Bazarov, *Ultrabright and Ultrafast III--V Semiconductor Photocathodes*, Phys. Rev. Lett. **112**, 097601 (2014).
[51] S. Uchiyama, Y. Takagi, M. Niigaki, H. Kan, and H. Kondoh, *GaN-Based Photocathodes with Extremely High Quantum Efficiency*, Appl. Phys. Lett. **86**, 103511 (2005).

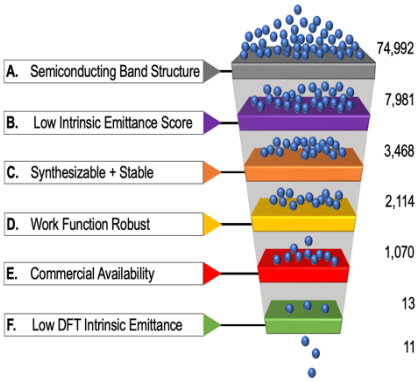
[52] A. Gassoumi, A. M. Alshehri, and N. Bouarissa, *Electronic Structure and Optical Response for Zn1−xBexSe*, Results Phys. **12**, 1294 (2019).
[53] O. I. Olusola, S. S. Oluyamo, and O. A. Ajayi, *Opto-Electronic Properties of Electrodeposited ZnTe Using Zinc Anode as Counter Electrode*, Mater. Sci. Semicond. Process. **123**, 105494 (2021).
[54] S. Venkatachalam, S. Agilan, D. Mangalaraj, and Sa. K. Narayandass, *Optoelectronic Properties of ZnSe Thin Films*, Mater. Sci. Semicond. Process. **10**, 128 (2007).
[55] *Growth of MgTe and Cd1−xMgxTe Thin Films by Molecular Beam Epitaxy*, J. Cryst. Growth **131**, 607 (1993).
[56] M. Isshiki and J. Wang, *II-IV Semiconductors for Optoelectronics: CdS, CdSe, CdTe*, in *Springer Handbook of Electronic and Photonic Materials*, edited by S. Kasap and P. Capper (Springer International Publishing, Cham, 2017), pp. 1–1.
[57] D. H. Dowell, *Sources of Emittance in RF Photocathode Injectors: Intrinsic Emittance, Space Charge Forces Due to Non-Uniformities, RF and Solenoid Effects*, ArXiv161001242 Phys. (2016).
[58] J. A. Berger, B. L. Rickman, T. Li, A. W. Nicholls, and W. A. Schroeder, *Excited-State Thermionic Emission in III-Antimonides: Low Emittance Ultrafast Photocathodes*, Appl. Phys. Lett. **101**, 194103 (2012).
[59] J. Paul, I. Bazarov, A. Galdi, R. Hennig, S. Karkare, and H. Padmore, *Computational Screening for Low Emittance Photocathodes*, Proc. 9th Int Part. Accel. Conf **IPAC2018**, 4 pages (2018).
[60] T. Li and W. A. Schroeder, *PbTe(111) Sub-Thermionic Photocathode: A Route to High-Quality Electron Pulses*, ArXiv170400194 Phys. (2017).
[61] S. H. Chou, J. Voss, I. Bargatin, A. Vojvodic, R. T. Howe, and F. Abild-Pedersen, *An Orbital-Overlap Model for Minimal Work Functions of Cesiated Metal Surfaces*, J. Phys. Condens. Matter **24**, 445007 (2012).
[62] G. Kresse and J. Furthmüller, *Efficient Iterative Schemes for Ab Initio Total-Energy Calculations Using a Plane-Wave Basis Set*, Phys. Rev. B **54**, 11169 (1996).
[63] P. E. Blöchl, *Projector Augmented-Wave Method*, Phys. Rev. B **50**, 17953 (1994).
[64] J. Heyd, G. E. Scuseria, and M. Ernzerhof, *Hybrid Functionals Based on a Screened Coulomb Potential*, J. Chem. Phys. **118**, 8207 (2003).
[65] W. Chen, J.-H. Pöhls, G. Hautier, D. Broberg, S. Bajaj, U. Aydemir, Z. M. Gibbs, H. Zhu, M. Asta, G. J. Snyder, B. Meredig, M. A. White, K. Persson, and A. Jain, *Understanding Thermoelectric Properties from High-Throughput Calculations: Trends, Insights, and Comparisons with Experiment*, J. Mater. Chem. C **4**, 4414 (2016).
[66] P. W. Tasker, *The Stability of Ionic Crystal Surfaces*, J. Phys. C Solid State Phys. **12**, 4977 (1979).
[67] T. T. Rantala, T. S. Rantala, V. Lantto, and J. Vaara, *Surface Relaxation of the (1010) Face of Wurtzite CdS*, Surf. Sci. **352–354**, 77 (1996).
[68] H. Xia, Q. Xia, and A. L. Ruoff, *BP at Megabar Pressures and Its Equation of State to 110 GPa*, J. Appl. Phys. **74**, 1660 (1993).
[69] K. Wilmers, T. Wethkamp, N. Esser, C. Cobet, W. Richter, V. Wagner, A. Waag, H. Lugauer, F. Fischer, T. Gerhard, M. Keim, and M. Cardona, *VUV Ellipsometry on Beryllium Chalcogenides*, Phys. Status Solidi B **215**, 15 (1999).
[70] Y. He, L. Jin, J. Zhang, B. Luo, K. Li, W. Wu, and J. Luo, *Thickness Dependence of Microstructure and Properties in Be2C Coatings as a Promising Ablation Material*, Matter Radiat. Extrem. **4**, 045403 (2019).

[71] M. P. Thompson, G. W. Auner, T. S. Zheleva, K. A. Jones, S. J. Simko, and J. N. Hilfiker, *Deposition Factors and Band Gap of Zinc-Blende AlN*, J. Appl. Phys. **89**, 3331 (2001).
[72] J. Li, K. B. Nam, M. L. Nakarmi, J. Y. Lin, H. X. Jiang, P. Carrier, and S.-H. Wei, *Band Structure and Fundamental Optical Transitions in Wurtzite AlN*, Appl. Phys. Lett. **83**, 5163 (2003).
[73] G. K. Rao, K. V. Bangera, and G. K. Shivakumar, *The Effect of Substrate Temperature on the Structural, Optical and Electrical Properties of Vacuum Deposited ZnTe Thin Films*, Vacuum **83**, 1485 (2009).
[74] P. K. Kalita, B. K. Sarma, and H. L. Das, *Structural Characterization of Vacuum Evaporated ZnSe Thin Films*, Bull. Mater. Sci. **23**, 313 (2000).
[75] K. W. Böer, *Cadmium Sulfide Enhances Solar Cell Efficiency*, Energy Convers. Manag. **52**, 426 (2011).
[76] R. C. Powell, N. -E. Lee, Y. -W. Kim, and J. E. Greene, *Heteroepitaxial Wurtzite and Zinc-blende Structure GaN Grown by Reactive-ion Molecular-beam Epitaxy: Growth Kinetics, Microstructure, and Properties*, J. Appl. Phys. **73**, 189 (1993).
[77] S. Adachi, *GALLIUM PHOSPHIDE (GaP)*, in *Optical Constants of Crystalline and Amorphous Semiconductors: Numerical Data and Graphical Information*, edited by S. Adachi (Springer US, Boston, MA, 1999), pp. 198–212.

Over 74,000 semiconducting materials are computationally screened to identify promising ultrahigh brightness photocathode materials for use in next-generation free electron lasers. This broad search results in the identification of novel materials that are predicted to be considerably brighter and more resistant to oxidation than the current state-of-the-art photocathode materials.

E. R. Antoniuk*, P. Schindler, W. A. Schroeder, B. Dunham, P. Pianetta, T. Vecchione, E. J. Reed*

Novel Ultrabright and Air-Stable Photocathodes Discovered from Machine Learning and Density Functional Theory Driven Screening



Supporting Information

Novel Ultrabright and Air-Stable Photocathodes Discovered from Machine Learning and Density Functional Theory Driven Screening

Evan R. Antoniuk[*], *Peter Schindler, W. Andreas Schroeder, Bruce Dunham, Piero Pianetta, Theodore Vecchione and Evan J. Reed*[*]

Supplementary Note 1: Background on Intrinsic Emittance Calculations

In this work, we adapt the methodology of Antoniuk et al. to calculate the intrinsic emittance of all 7,981 semiconducting materials identified in this work.[25] Within this approach, the intrinsic emittance, ε_{int}, is calculated as:

$$\varepsilon_{int}(\omega,T) = \frac{\hbar}{mc}\sqrt{\sum_i w_i(\vec{k},\omega,T)k_{x,i}^2} \quad \text{(S1)}$$

where w_i represents the relative probability that the i^{th} possible optical transition will result in emitting an electron with wavevector, k_x. The weight, w_i is then calculated as:

$$w_i(\vec{k},\omega,T) = \frac{1}{N}w_{i,kpt}(\vec{k}) \times w_{i,opt}(\vec{k},\omega,T) \times w_{i,escape}(\vec{k}) \quad \text{(S2)}$$

where N is a normalization factor and $w_{i,kpt}(\vec{k})$ is the number of symmetry equivalent k-points with the same value of k_x. $w_{i,opt}(\vec{k},\omega,T)$ is the photoexcitation probability of excitation between a final conduction band state, $\psi_{\vec{k},c}$, and an initial valence band state, $\psi_{\vec{k},v}$, and is given by:

$$w_{i,opt}(\vec{k},\omega,T) = \langle\psi_{\vec{k},c}|\vec{p}|\psi_{\vec{k},v}\rangle^2 \times \delta[E_c(\vec{k}) - E_v(\vec{k}) - \hbar\omega] \times [f(E_v,T) - f(E_c,T)] \quad \text{(S3)}$$

where $f(E,T)$ is the Fermi-Dirac distribution of a state with energy, E, and an electronic temperature, T, δ is the Dirac delta function, and $\vec{p}$ is the momentum operator of the optical field. $w_{i,escape}(\vec{k})$ is the probability of the photoexcited electron being emitted from the surface of the photocathode. Since all three of the terms in Equation S2 depend on $\vec{k}$, evaluating $w_{i,kpt}(\vec{k})$ requires a calculation of the electronic dispersion of the material, $E(\vec{k})$. Evaluating $w_{i,opt}(\vec{k},\omega,T)$ requires an additional calculation of the matrix elements of the photoexcitation, $H_{cv} = \langle\psi_{\vec{k},c}|\vec{p}|\psi_{\vec{k},v}\rangle$. Finally, $w_{i,escape}(\vec{k})$ is then given by,

$$w_{i,escape}(\vec{k}) = \frac{4k_{z,in}k_{z,out}}{(k_{z,in}+k_{z,out})^2} \quad \text{(S4)}$$

where $k_{z,in}$ is the z-component of the crystal momentum wavevector inside the photocathode and $k_{z,out}$ is the z-component of the wavevector of the emitted electron. $k_{z,out}$ is dependent on the work function of the surface of the photocathode, ϕ, through the expression:

$$k_{z,out} = \sqrt{\frac{2m}{\hbar^2}(E-\phi) - k_{x,out}^2 - k_{y,out}^2} \quad \text{(S5)}$$

In summary, determination of the intrinsic emittance of a photocathode material with Equation S1 requires, at minimum, some representation of ϕ, H_{cv}, and $E(\vec{k})$ of the photocathode material. We refer interested readers to Reference [25] for a rigorous derivation of these expressions. We note that this photoemission model assumes a resonant electron emission process, whereby the emitted electron is assumed to be in the same conduction band state that it was photoexcited into. This photoemission model therefore neglects the thermalization of excited electrons into the conduction band minimum, as well as the transport of electrons to the surface for emission which could be relevant in materials with large skin depths. Additionally, this model assumes that the photoemission is dominated by bulk electronic states, which we expect to be valid in materials with skin depths of at least 10nm.

Supplementary Note 2: Discussion of Intrinsic Emittance Score

In Section 2.2, we employ a number of approximations to allow Equation S1 to be evaluated with only the data that is available on the Materials Project database. First, we assume the photoexcitation matrix elements, H_{cv}, to be unity for all pairs of conduction band states and valence band states. This approximation assumes that all pairs of conduction and valence band states that obey $E_c(\vec{k}) - E_v(\vec{k}) = \hbar\omega$ will have an equal probability of being excited by a photon of energy, $\hbar\omega$. We represent the electronic dispersion of the material, $E(\vec{k})$, with the electronic band structures pulled from the Materials Project database. We assume a weight of $w_{i,kpt}(\vec{k})$=1 for every k-point in the electronic band structure. We also note that these band structures are calculated with the PBE functional and are expected to underestimate the experimental band gap by approximately 40%, with a mean absolute error of 1.0eV.[31,58] Following the method in Ref. [25], we use a lifetime broadening of 0.20eV for evaluation of δ in Equation S3. We also take the transverse direction to be along the x-axis. The photon energy dependence of $\varepsilon_{int}(\omega)$ is captured by calculating $\varepsilon_{int}(\omega)$ with photon energies ranging from $\hbar\omega = \phi$, up to $\hbar\omega = \phi + 5eV$, with a step size of 0.05eV.

Evaluation of Equation S1 also requires a work function value, which is not known for each material in our database a priori. However, there are a number of physical and computational considerations that constrains our initial choice of work function value. First, the work function must be non-negative since it physically represents the energy required to remove an electron from the material. Secondly, it is preferential at the initial stage of the screening process to have the work function to be lower in energy than the conduction band minimum. Placing the work function below the conduction band minimum allows all conduction band states to potentially contribute to photoemission (Equation S5), which increases the likelihood that a material can exhibit low intrinsic emittance. The result of this choice is that we identify an upper limit to the number of materials that can have low intrinsic emittance. This is desirable for an early stage of the screening process because it identifies all materials that have the potential for low intrinsic emittance and prevents promising candidates from being filtered out due to a more restrictive choice of work function. Thirdly, we note that the calculated intrinsic emittance does not change when the work function is less than the conduction band minimum, when assuming constant photoexcitation probability (Equation S1-S5). Therefore, placing the work function far below the conduction band minimum is computationally inefficient since no electron emission will occur for photon energies less than the band gap, i.e. $\hbar\omega < E_{CBM} - E_{vBM}$. Taking all of these considerations into account, we take the work function of each photocathode material to be $\phi = max(E_{CBM} - 0.5eV, 0eV)$, where E_{CBM} is the energy of the conduction band minimum, relative to the Fermi level. This choice ensures that the work function is always non-negative

and lower in energy than the conduction band minimum. The choice of taking ϕ to be 0.5eV below the conduction band minimum allows for electrons excited into conduction band minima states to be emitted in the case that $k_{x,out}$ or $k_{y,out}$ are non-zero (Equation S5).

Although it is possible to use our machine learning model to predict ϕ to use in our initial screening, the main complication that arises is that we do not know which Miller index surface termination is the most stable for each material in our database. Choosing $\phi = max(E_{CBM} - 0.5eV, 0eV)$ identifies all materials that can achieve low intrinsic emittance by initially using an optimistic choice of ϕ, which we then validate later in our screening with DFT calculations on the experimentally reported stable surface termination.

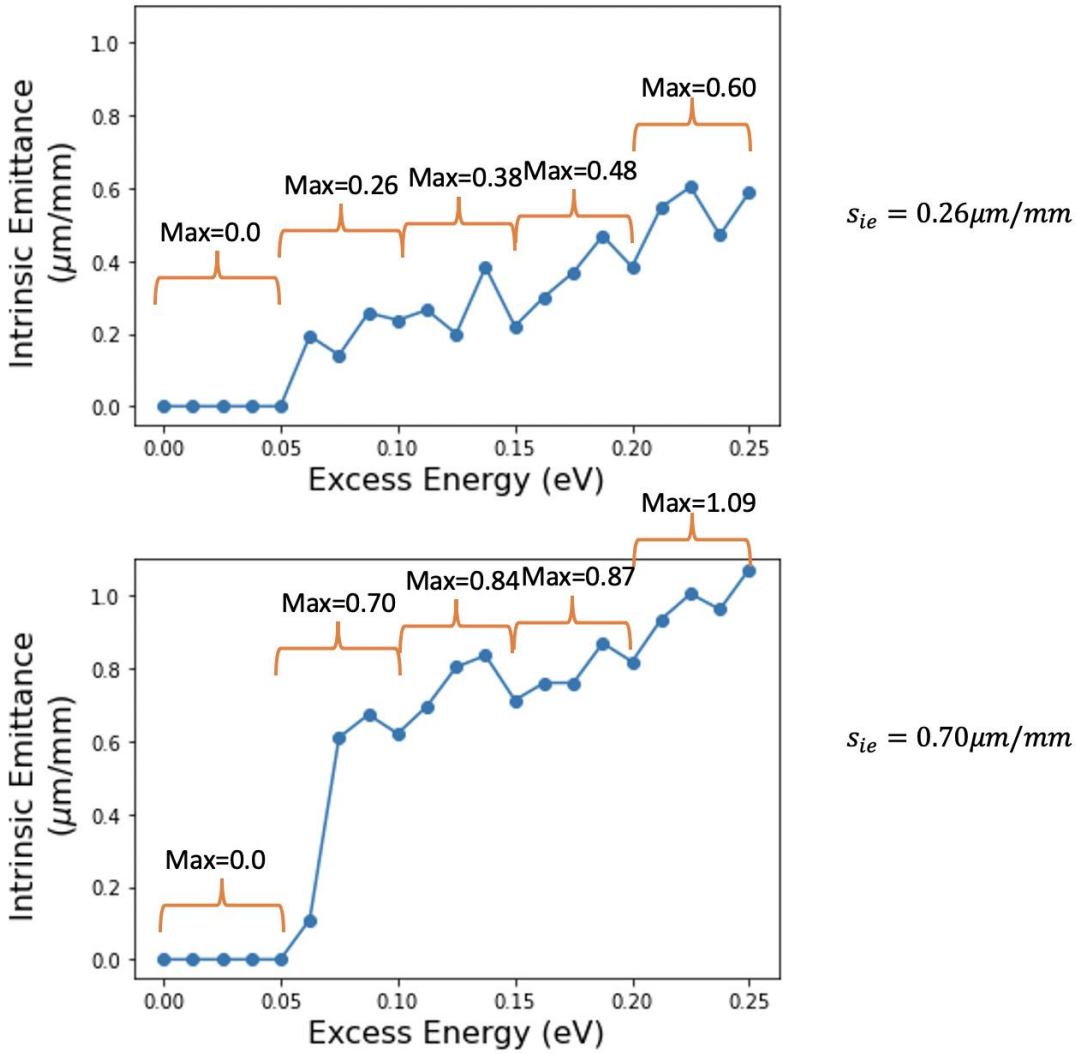


Figure S1. Procedure for calculating s_{ie} for hypothetical intrinsic emittance data. First, we determine the maximum intrinsic emittance value for a bin size of 0.05eV. s_{ie} is then the minimum of all of these bins, giving $s_{ie} = 0.26\mu m/mm$ (top) and $s_{ie} = 0.70\mu m/mm$ (bottom). Notably, the binning prevents the $\varepsilon_{int} = 0.10\mu m/mm$ point on the bottom plot to give rise to a low s_{ie}. This increases the robustness of our screening workflow by preventing fortuitously low ε_{int} values from giving rise to low intrinsic emittance scores.

After employing these approximations, we can then use Equation S2 to calculate $\varepsilon_{int}(\omega)$. The intrinsic emittance score (s_{ie}) that we use to identify low intrinsic emittance materials is then calculated from $\varepsilon_{int}(\omega)$. To calculate s_{ie}, we bin all non-zero values of $\varepsilon_{int}(\omega)$ with an interval of 0.05eV by recording the maximum intrinsic emittance in each bin. The value of s_{ie} is then taken to be the lowest of these binned values (Figure S1).

Formulating s_{ie} in this way provides a number of useful properties that aid in the robust identification of low intrinsic emittance materials. First, the inclusion of the 0.05eV sliding window ensures that the low emittance materials discovered from our screening are able to exhibit low intrinsic emittance for a range of photon energies, rather than requiring an extremely precise incident photon energy. Additionally, s_{ie} is invariant to shifts in the band gap, assuming the vacuum level is located below the conduction band minimum. Although different choices of exchange-correlation functionals will impact the value of E_{CBM}, such shifts in the band gap will simply horizontally translate a plot of intrinsic emittance vs. photon energies (Figure S1), without changing the curvature of the plot. Since we calculate the intrinsic emittance score by recording the maximum intrinsic emittance in each 0.05eV bin, the intrinsic emittance score will be unaffected by shifts in E_{CBM}. This allows us to accurately identify low intrinsic emittance materials despite the well-known underestimation of band gaps calculated with the generalized gradient approximation PBE functional.[26,27] Finally, s_{ie} removes the photon energy dependence of $\varepsilon_{int}(\omega)$, allowing the photoemission properties of different materials to be directly compared without requiring specification of a particular photon energy.

The loose k-point sampling that is inherent to the Materials Project band structures may have two negative effects on our screening results: i) discovering materials with poor performance (overestimating emittance) or ii) accidentally eliminating promising materials (underestimating emittance). In the first scenario, we emphasize that for all 17 candidates that we study in detail in this work, we perform DFT validations with a dense, uniform k-point mesh. These calculations provide validation for the photoemission properties of these top candidates in a manner that is independent of the limitations of the MP band structures. Among these 17 materials tested, we found that 15/17 (88%) of the low emittance materials discovered with the MP band structures retained their low emittance with dense k-point calculations. As a tool for accelerating materials discovery, we find that this is a remarkably high rate of success for finding promising candidates. Although our screening identifies a high proportion of successful materials, the 2 misclassified materials highlights the importance of the DFT validations that we perform following the screening process. In the case of the second scenario where emittance is underestimated, it is nearly impossible to quantify how many materials are left undiscovered. However, we do not see any significant underestimation of the MP predicted emittance in any of the 17 validated materials (Figure S4).

Due to the proportional relationship between ε_{int} and k_x^2 in Equation S1, we note that the value of s_{ie} can be limited by the k-point density of the DFT calculation. For example, the smallest non-zero value of k_x for an electronic structure calculation on a uniform 16x16x16 k-point mesh would be $\frac{1}{15}\cdot\frac{\pi}{a}$, giving the smallest possible non-zero value of ε_{int} to be $\frac{\hbar}{mc}\sqrt{(\frac{\pi}{15a})^2}$. For a typical lattice constant of $a = 5.0$Å, this corresponds to a minimum intrinsic emittance of $0.16\mu m/mm$. Therefore, for materials with small values of s_{ie}, the value of s_{ie} calculated from

Materials Project band structures may be overestimated if it is limited by the k-point density of the band structure calculation. Nevertheless, this effect does not prevent s_{ie} from distinguishing between materials with high intrinsic emittance and low intrinsic emittance.

Supplementary Note 3: Calculating Range of Work Function Values with Low Intrinsic Emittance:

To determine the range of hypothetical work function values that can give rise to low intrinsic emittance, we calculate s_{ie} with the method described in Supplementary Note 2. The work function dependence of s_{ie} is determined by calculating s_{ie} with hypothetical work function values ranging from $\phi = max(E_{CBM} - 0.5eV, 0eV)$ up to $\phi + 5eV$, with a step size of 0.25eV. Once the work function dependence of $s_{ie}(\phi)$ has been calculated, we find the largest continuous range of work function values, ϕ, that give $s_{ie}(\phi) \leq 0.3\mu m/mm$ (**Figure S2**). In both Sections 3 and 4.1, we screen for the materials that have a range of work function values that is at least 1.0eV. This criteria increases the robustness of our screening workflow by ensuring that a low s_{ie} value is maintained over a relatively broad range of hypothetical work function values, rather than just the initial hypothetical work function value of $\phi = max(E_{CBM} - 0.5eV, 0eV)$ used in Section 2.2.

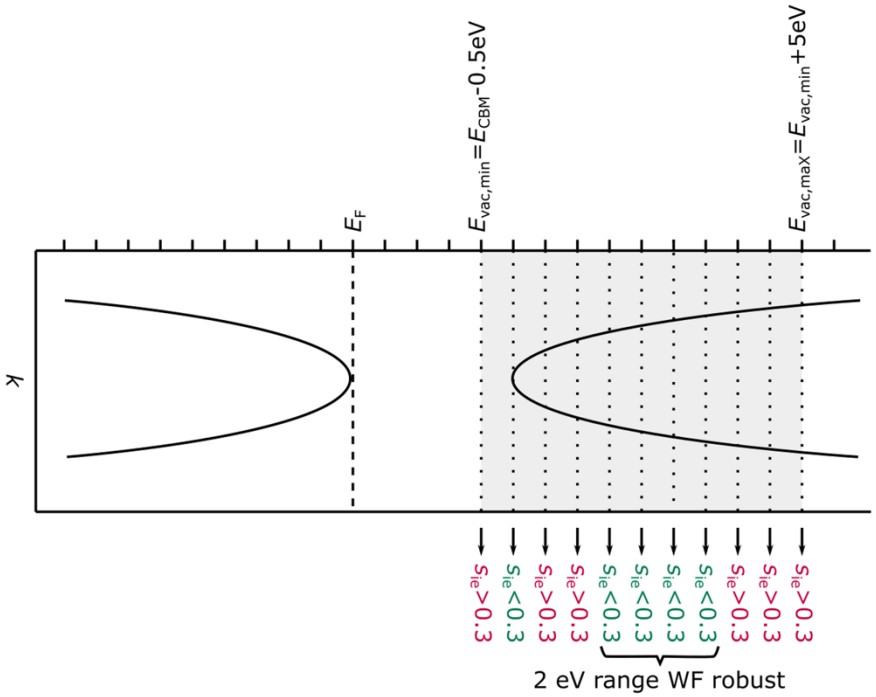


Figure S2. Procedure for determining the range of work function values that give $s_{ie}(\phi) \leq 0.3\mu m/mm$ for a hypothetical band structure. The spacing between vertical dotted lines is 0.50eV.

Table S1. Chemical formulas of the synthesizable, low intrinsic emittance photocathode materials discovered in Section 2.3 that belong to known chemical families of photocathode materials. We consider a material to belong to a family only if all atoms in the formula are represented in the family name. For example, KNaTe is considered an alkali telluride, but KCuTe is not. The remaining 2,078 of the 2,114 materials do not fall into any known family.

Known Photocathode Family	**Materials In Family**	**# Materials in Family**
Alkali Tellurides *(Cs_2Te)*	Li_2Te (mp-2530), CsTe (mp-8361), K_2Te (mp-1747), Cs_2Te (mp-573763), KTe (mp-2072), Rb_2Te (mp-441), CsNaTe (mp-5339), Na_2Te (mp-2784), KLiTe (mp-4495), KNaTe (mp-8755), RbTe (mp-8360)	11
Alkali Antimonides *(Cs_3Sb, K_2CsSb)*	Cs_3Sb (mp-10378), Li_3Sb (mp-2074), Rb_3Sb (mp-16319), RbSb (mp-10487), RbSb (mp-7444), K_3Sb (mp-10159), $NaLi_2Sb$ (mp-5077), CsSb (mp-573514), CsK_2Sb (mp-581024), KSb (mp-1536), KNa_2Sb (mp-15724)	11
III-V Semiconductors (GaN,GaAs)	AlAs (mp-2172), AlN (mp-1700), GaN (mp-830), GaP (mp-2490), InN (mp-22205), BP (mp-1479), AlSb (mp-1018100), AlSb (mp-2624), GaSb (mp-1156), GaAs (mp-2534), GaSb (mp-1018059), $AlGa_3N_4$ (mp-1019508), AlP (mp-1550), InP (mp-966800)	14

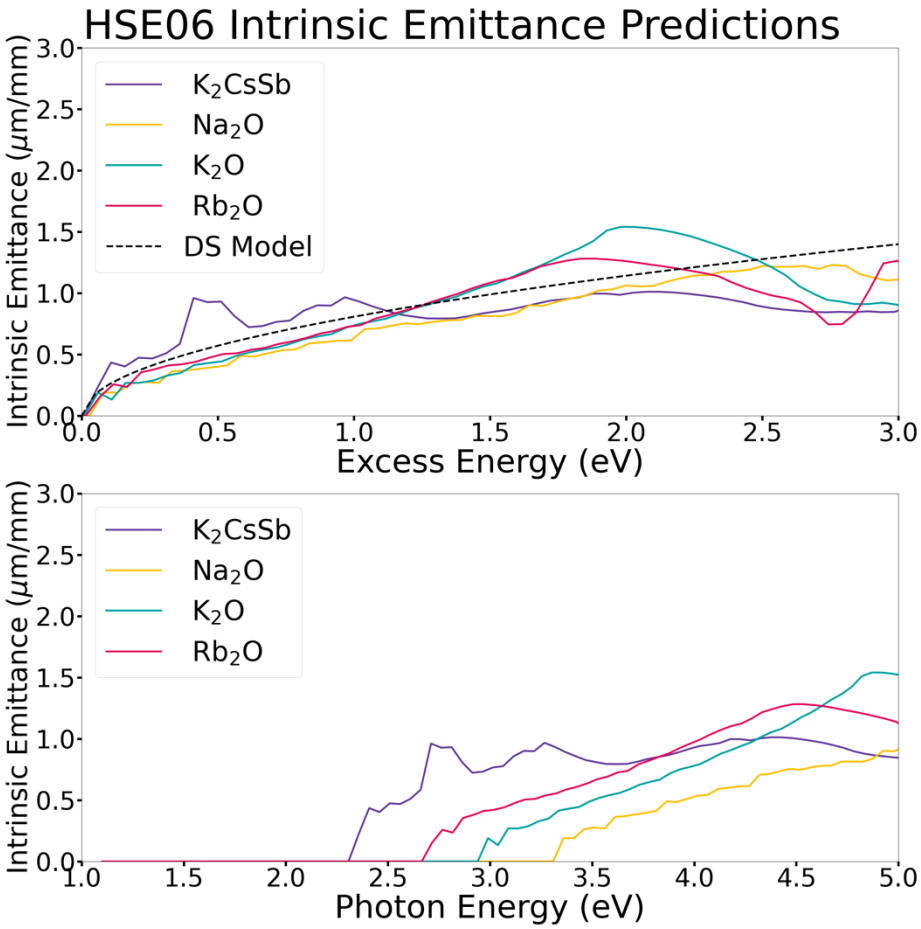


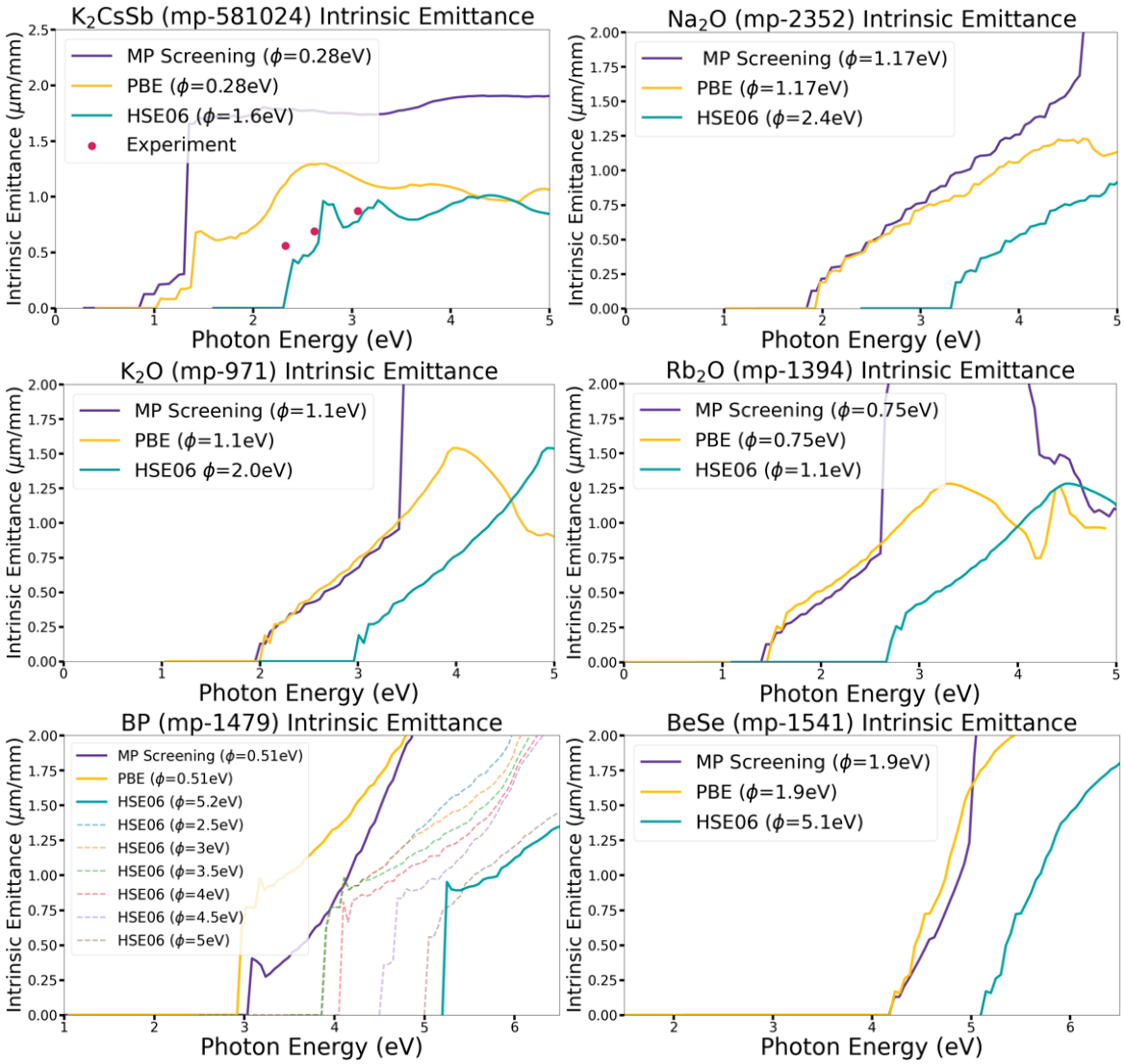
Figure S3. Calculated intrinsic emittance for K_2CsSb, Na_2O, K_2O and Rb_2O plotted against the energy above the photoemission threshold (top) and against the incident photon energy (bottom). For all 4 materials, the work function is calculated with the alkali-terminated (111) surface. For K_2CsSb, the (111) surface is taken to be Cs terminated. The Dowell-Schmerge (DS) model with an electron effective mass of $m_e^* = 1.0m_e$ is also plotted for comparison.[36]

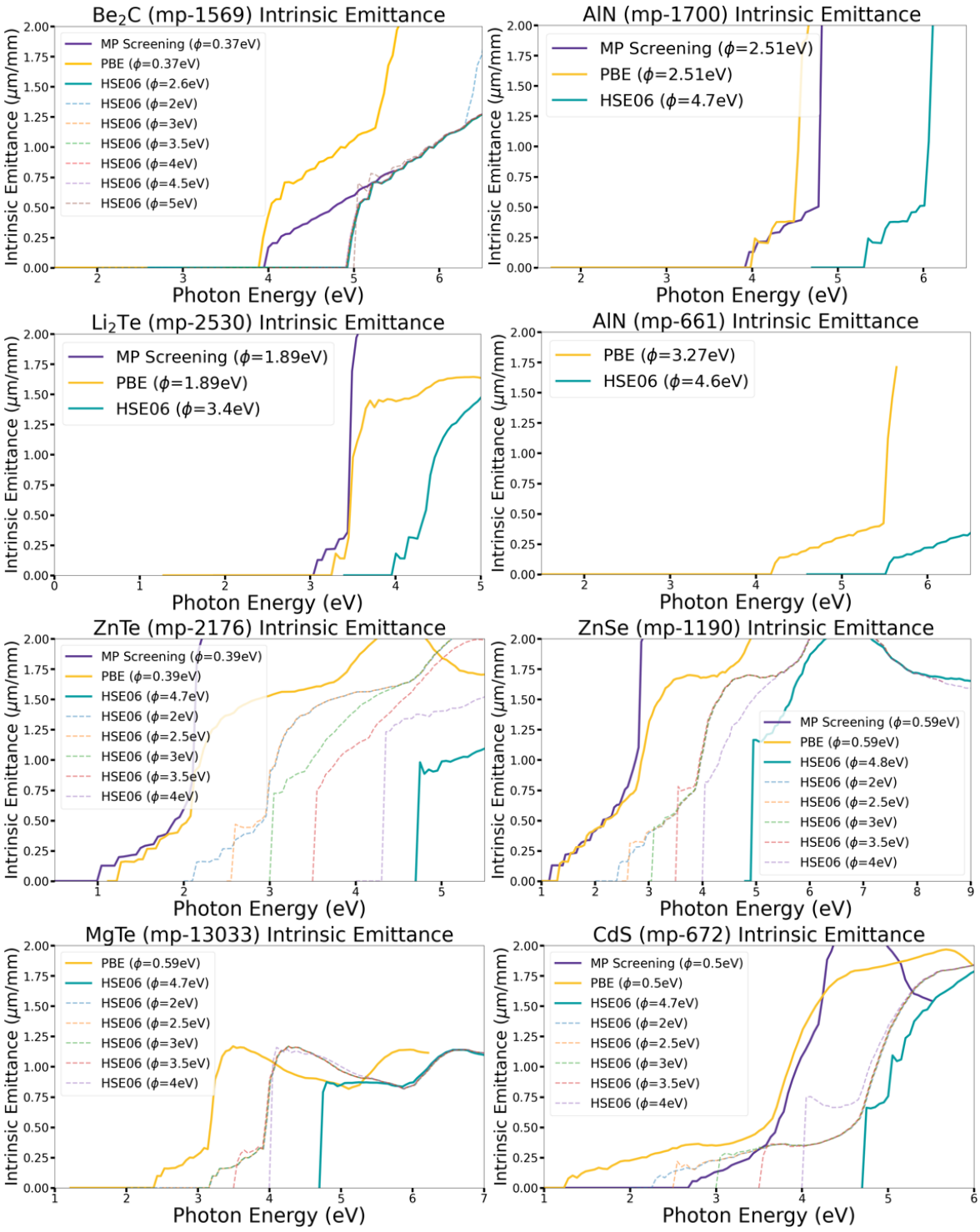
Table S2. Intrinsic emittance of all materials studied with DFT calculations. The "DFT ϕ" column indicates if the material has low intrinsic emittance ($\leq 0.30 \mu m/mm$) over a 0.05eV range of incident photon energies is with the DFT calculated work function value (ϕ). The DFT calculated work function value is with respect to the experimentally observed stable surface termination (see Methods). The "Optimized WF" column indicates if the material has low intrinsic emittance ($\leq 0.30 \mu m/mm$) over a 0.05eV range of incident photon energies with any work function value. The DFT calculated work function of each material is also given, along with the Miller index and terminating atom of the surface. Band gaps indicated by a * indicate an electronic band gap. Otherwise, experimental and computed band gaps refer to the optical band gap of the material. Electron effective masses are obtained from Materials Project band structures.

Formula (MP ID)	Structure Type	DFT ϕ (eV)	$\varepsilon_{int} \leq 0.30 \mu m/mm$ (DFT WF)	$\varepsilon_{int} \leq 0.30 \mu m/mm$ (Optimized WF)	HSE06 Band Gap (eV)	Exp. Band Gap (eV)	Electron Effective Mass (Exp.) (m_e)
K_2CsSb (mp-581024)	Face-centered cubic	1.6 (Cs,111)	No	Yes	1.45 Direct	1.2[46]	0.18
Na_2O (mp-2352)	Anti-fluorite	2.4 (Na,111)	Yes	Yes	3.26 Direct	-	0.35
K_2O (mp-971)	Anti-fluorite	2.0 (K,111)	Yes	Yes	2.96 Indirect	-	0.41
Rb_2O (mp-1394)	Anti-fluorite	1.1 (Rb,111)	Yes	Yes	2.52 Indirect	-	0.36
BP (mp-1479)	Zinc blende	5.2 (110)	No	No	2.08* Indirect	2.0*[68]	1.11
BeSe (mp-1541)	Zinc blende	5.1 (110)	Yes	Yes	5.15 Indirect	5.55[69]	0.28
Be_2C (mp-1569)	Anti-fluorite	2.6 (Be,111)	No	No	1.91* Indirect	1.9*[70]	0.24
AlN (mp-1700)	Zinc blende	4.7 (110)	Yes	Yes	5.35 Indirect	5.34[71]	0.34
Li_2Te (mp-2530)	Anti-fluorite	3.4 (Li,111)	Yes	Yes	3.22 Indirect	-	0.31
AlN	Wurtzite	4.6 $(10\bar{1}0)$	Yes	Yes	5.41 Direct	6.12[72]	0.31

(mp-661)							
ZnTe (mp-2176)	Zinc-blende	4.7 (110)	No	Yes	1.95 Direct	2.26[73]	0.13
ZnSe (mp-1190)	Zinc-blende	4.8 (110)	No	Yes	2.24 Direct	2.7[74]	0.14
MgTe (mp-13033)	Zinc-blende	4.7 (110)	No	Yes	3.09 Direct	~3.0[55]	-
CdS (mp-672)	Wurtzite	4.7 $(10\bar{1}0)$	No	Yes	2.12 Direct	2.4[75]	0.17
Na_2Te (mp-2784)	Anti-fluorite	3.4 (Na,111)	No	Yes	2.78 Direct	-	0.24
GaN (mp-830)	Zinc-blende	5.0 (110)	No	Yes	2.80 Direct	3.21[76]	0.19
GaP (mp-2490)	Zinc-blende	4.6 (110)	No	Yes	2.36 Indirect	2.74[77]	0.17

Figure S4. Comparison of intrinsic emittance predictions made using the Materials Project band structures described in Section 2.2 (purple), a PBE calculation with a uniform k-point mesh (yellow) and our PBE calculations shifted to the HSE06 band gap (teal). For materials that exhibit low intrinsic emittance only with an optimized work function (Table S2), the intrinsic emittance is plotted over a range of hypothetical work function values to illustrate the potential for low intrinsic emittance. The intrinsic emittance plotted for the hypothetical work function values are calculated with the band structure shifted to the HSE06 band gap. For K_2CsSb, the experimentally measured intrinsic emittance values are shown. [31] The DFT work function is calculated with respect to be the (111) cation terminated surface for all antifluorite structures, the (110) surface for all zinc blende structures, $(10\bar{1}0)$ for all wurtzite structures and Cs-terminated (111) for K_2CsSb.




Be2C (mp-1569) Intrinsic Emittance
MP Screening (ϕ=0.37eV)
PBE (ϕ=0.37eV)
HSE06 (ϕ=2.6eV)
HSE06 (ϕ=2eV)
HSE06 (ϕ=3eV)
HSE06 (ϕ=3.5eV)
HSE06 (ϕ=4eV)
HSE06 (ϕ=4.5eV)
HSE06 (ϕ=5eV)
AlN (mp-1700) Intrinsic Emittance
MP Screening (ϕ=2.51eV)
PBE (ϕ=2.51eV)
HSE06 (ϕ=4.7eV)
Li2Te (mp-2530) Intrinsic Emittance
MP Screening (ϕ=1.89eV)
PBE (ϕ=1.89eV)
HSE06 (ϕ=3.4eV)
AlN (mp-661) Intrinsic Emittance
PBE (ϕ=3.27eV)
HSE06 (ϕ=4.6eV)
ZnTe (mp-2176) Intrinsic Emittance
MP Screening (ϕ=0.39eV)
PBE (ϕ=0.39eV)
HSE06 (ϕ=4.7eV)
HSE06 (ϕ=2eV)
HSE06 (ϕ=2.5eV)
HSE06 (ϕ=3eV)
HSE06 (ϕ=3.5eV)
HSE06 (ϕ=4eV)
ZnSe (mp-1190) Intrinsic Emittance
MP Screening (ϕ=0.59eV)
PBE (ϕ=0.59eV)
HSE06 (ϕ=4.8eV)
HSE06 (ϕ=2eV)
HSE06 (ϕ=2.5eV)
HSE06 (ϕ=3eV)
HSE06 (ϕ=3.5eV)
HSE06 (ϕ=4eV)
MgTe (mp-13033) Intrinsic Emittance
PBE (ϕ=0.59eV)
HSE06 (ϕ=4.7eV)
HSE06 (ϕ=2eV)
HSE06 (ϕ=2.5eV)
HSE06 (ϕ=3eV)
HSE06 (ϕ=3.5eV)
HSE06 (ϕ=4eV)
CdS (mp-672) Intrinsic Emittance
MP Screening (ϕ=0.5eV)
PBE (ϕ=0.5eV)
HSE06 (ϕ=4.7eV)
HSE06 (ϕ=2eV)
HSE06 (ϕ=2.5eV)
HSE06 (ϕ=3eV)
HSE06 (ϕ=3.5eV)
HSE06 (ϕ=4eV)
Intrinsic Emittance (μm/mm)
Photon Energy (eV)

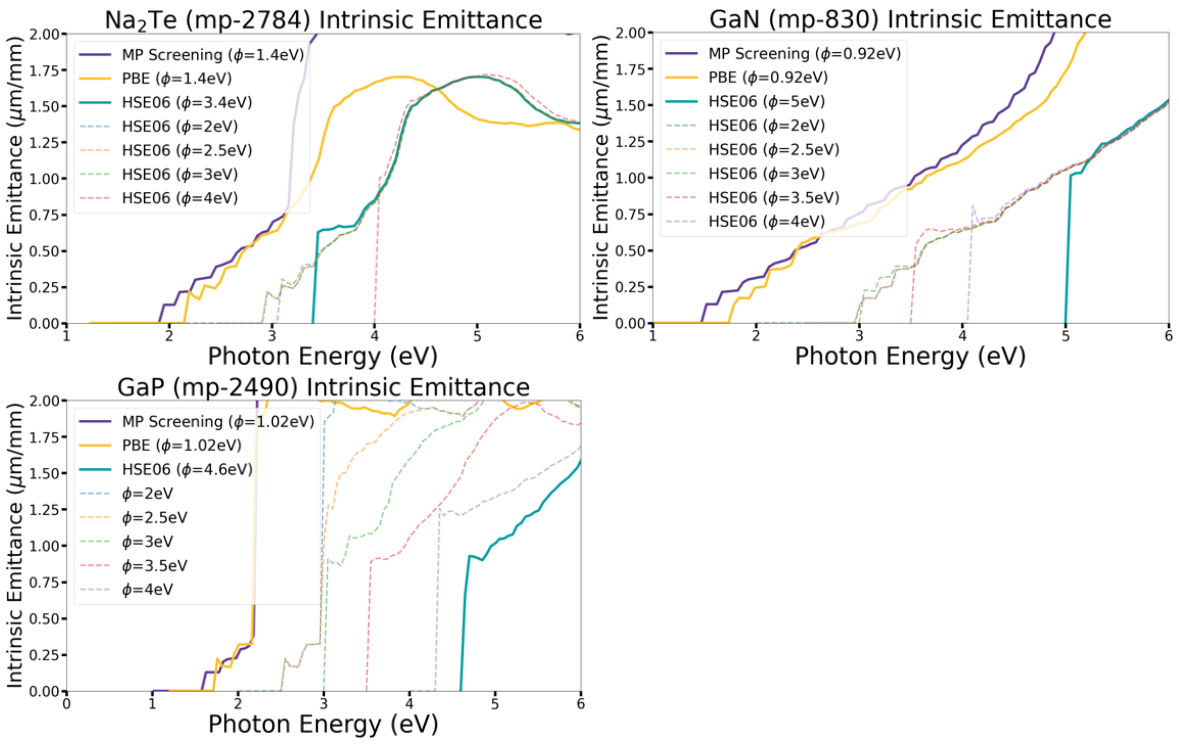




Figure S5. Intrinsic emittance scores (s_{ie}) calculated for 2114 low intrinsic emittance materials identified in Section 2.2. The work function plotted for each material is the minimum work function predicted by the machine learning model over all possible Miller indices up to an index of 1 and all possible termination atoms. A linear fit (y=0.0009x + 0.136) to all data points is indicated by the red line. The Pearson correlation coefficient between the two quantities is 0.010, indicating a lack of significant correlation.

Table S3. Number of materials within intrinsic emittance score ranges as shown in Figure 6. The percentage shown in parentheses is calculated with respect to the number of materials in the "All Materials" row. A total of 215 out of 7,981 materials experienced errors in their high-throughput calculation of intrinsic emittance scores and are omitted here.

Intrinsic Emittance Score ($\mu m/mm$)	**# Direct Band Gap Materials**	**# Indirect Band Gap Materials**	**# Total Materials**
<0.05	79 (3.9%)	171 (3.0%)	250 (3.2%)
<0.10	417 (20.5%)	675 (11.8%)	1092 (14.1%)
<0.20	902 (44.4%)	1645 (28.7%)	2547 (32.8%)
<0.30	1198 (59.0%)	2222 (38.7%)	3420 (44.0%)
<0.40	1283 (63.2%)	2453 (42.8%)	3736 (48.1%)
<0.50	1331 (65.6%)	2646 (46.1%)	3977 (40.4%)
All Materials	**2030**	**5736**	**7766**

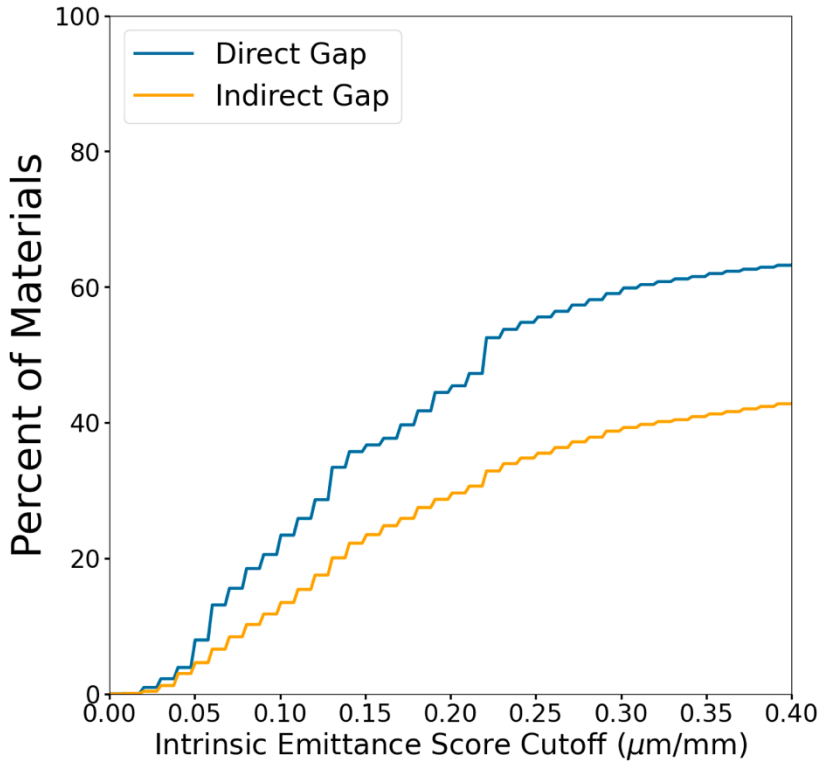


Figure S6. Percentage of 7,981 materials identified in Section 2.2 with an intrinsic emittance score below a cutoff value, plotted for indirect and direct band gap materials.

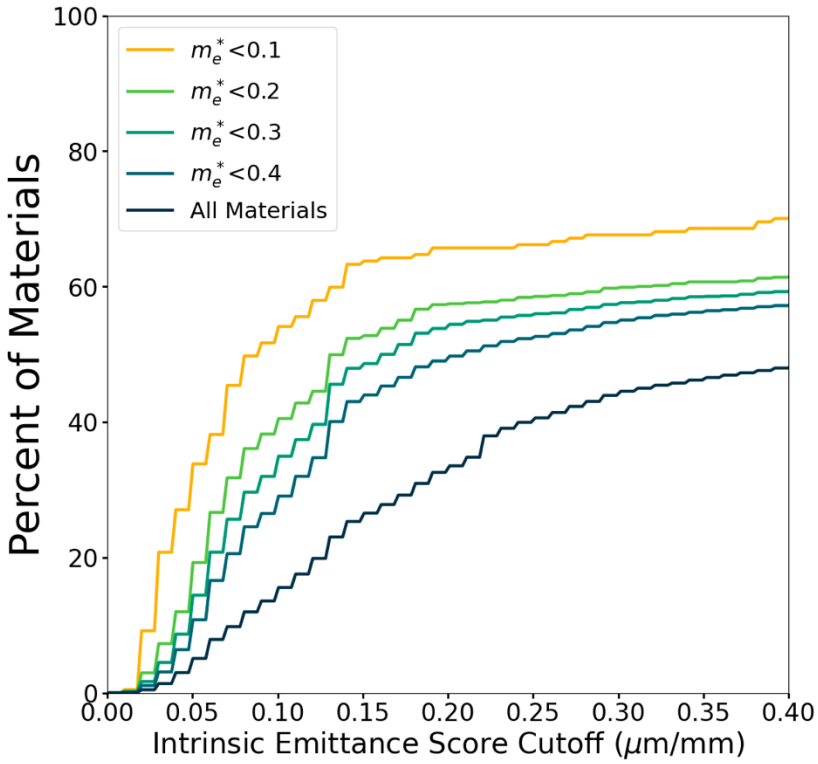


Figure S7. Percentage of the 7,981 materials identified in Section 2.2 with an intrinsic emittance score below a cutoff value, plotted for multiple electron effective mass ranges. Materials with negative electron effective masses are excluded.

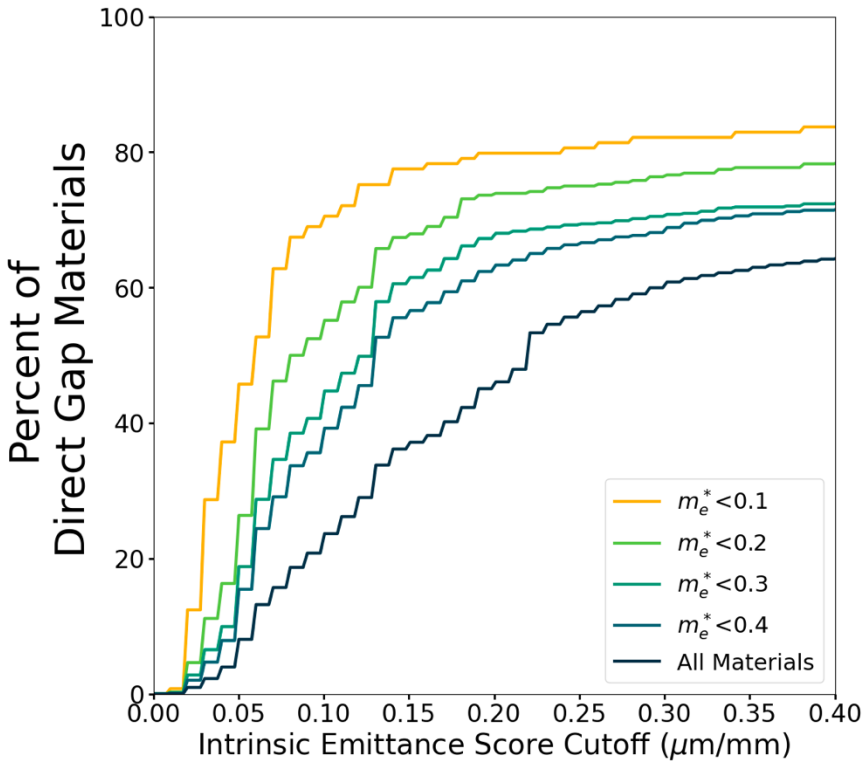


Figure S8. Percentage of direct band gap materials with an intrinsic emittance score below a cutoff value, plotted for multiple electron effective mass ranges. Materials with negative electron effective masses are excluded.

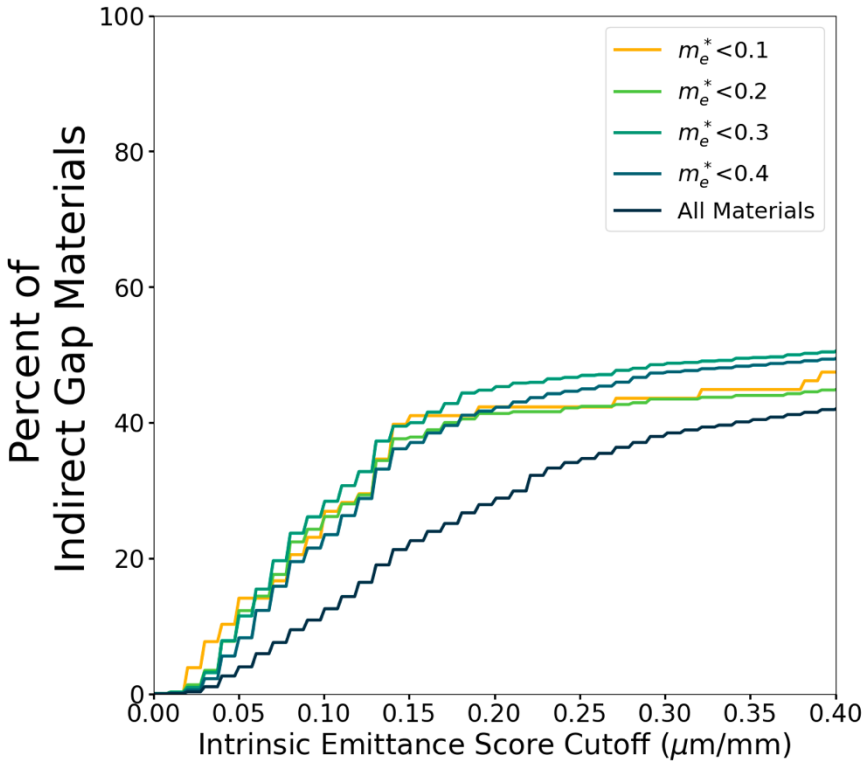


Figure S9. Percentage of indirect band gap materials with an intrinsic emittance score below a cutoff value, plotted for multiple electron effective mass ranges. Materials with negative electron effective masses are excluded.

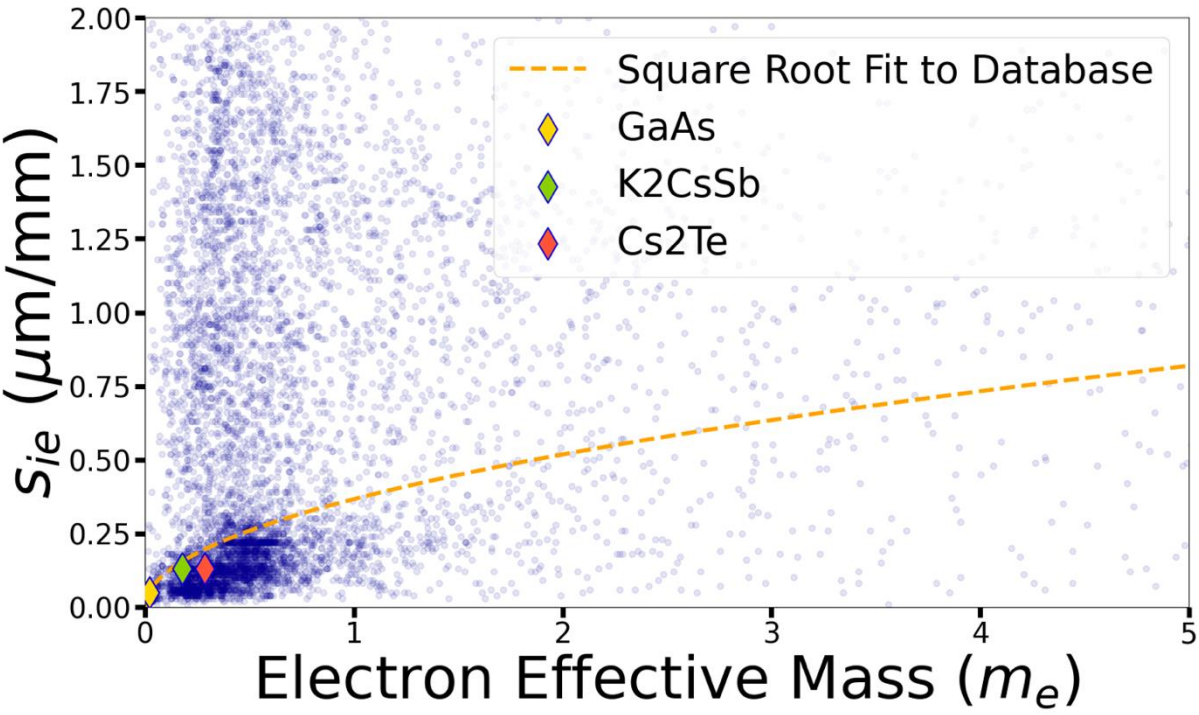


Figure S10. Calculated intrinsic emittance scores (s_{ie}) plotted against the electron effective mass for the 7,981 semiconducting candidate materials in Section 2.2. A square root law of the form $y = \sqrt{ax}$ is fit to the data and plotted in yellow. The mean absolute error between this square root law and the data points is $0.53 \mu m/mm$, whereas the standard deviation in intrinsic emittance scores is $0.66 \mu m/mm$.

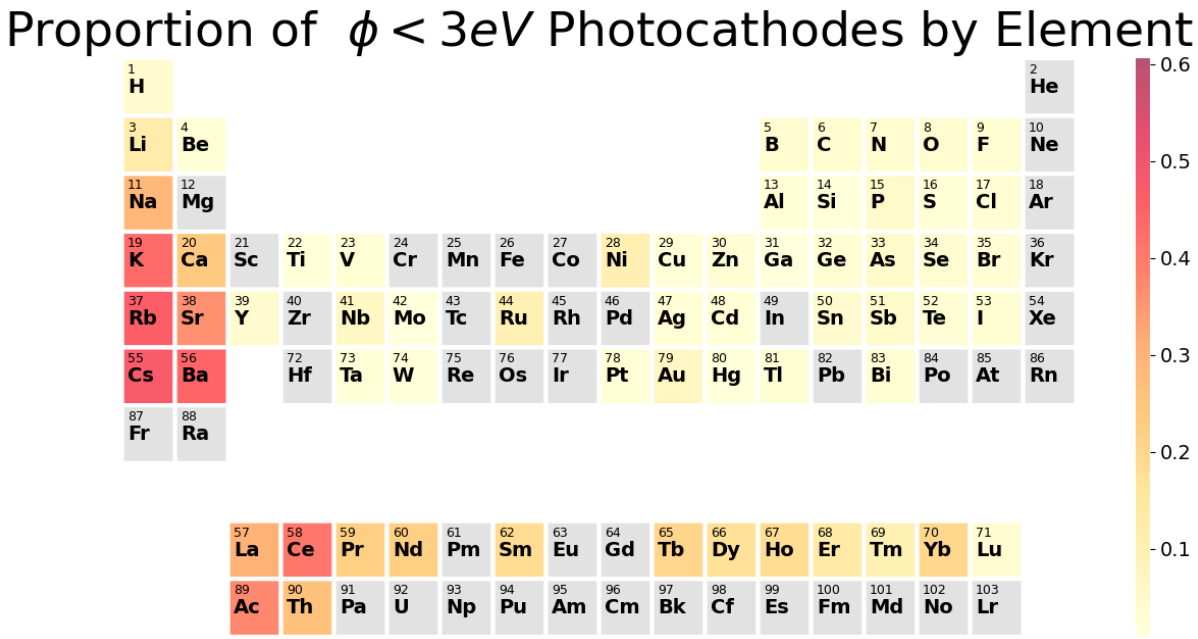


Figure S11. Fraction of the 2,114 low emittance materials identified in Section 2.3 with at least one surface termination with a work function $< 3eV$, colored by the topmost element of the surface. Elements that do not appear in the database are colored grey.